Modeling and simulation of multiple bubble entrainment and interactions with two dimensional vortical flows

Justin Finn,[1, a)] Ehsan Shams,[1, b)] and Sourabh V. Apte[1, c)]

School of Mechanical, Industrial, and Manufacturing Engineering

Oregon State University, Corvallis, OR 97331.

(Dated: 5 November 2010)

Simulations of bubble entrainment and interactions with two dimensional vortical flows are preformed using a Discrete Element Model (DEM). In this Eulerian-Lagrangian approach, solution to the carrier phase is obtained using direct numerical simulation whereas motion of subgrid bubbles is modeled using Lagrangian tracking. The *volumetric displacement* of the fluid by the finite size of the bubbles is modeled along with interphase momentum-exchange for a realistic coupling of the bubbles to the carrier phase. In order to assess the importance of this *volumetric coupling effect* even at low overall volume loading, simulations of few microbubbles entrained in a traveling vortex tube is studied in detail. The test case resembles the experiments conducted by Sridhar & Katz [JFM, 1999] on bubble-entrainment in vortex-rings. It is shown that under some conditions, the entrainment of eight small bubbles, $1,100\mu m$ or less in diameter, result in significant levels of vortex distortion when modeled using the volumetric coupling effect. Neglecting these effects; however, does not result in any vortex distortion due to entrained bubbles. The non-dimensionalized vortex-strength versus bubble settling locations are compared with experimental data to show collapse of the data along the trends observed in experiments only when the volumetric effects are modeled. Qualitative and quantitative assessments of this distortion observed with volumetric coupling are made using three methods; bubble induced vortex asymmetry, relative change in the decay of angular momentum, and relative change in the peak vorticity. It is found that in all cases the *volumetric* effects result in a relative *increase* of the vortex decay rate. The concept of a relative reaction force, defined as the ratio of net bubble to fluid reaction to the local driving force of the vortex, is introduced to analyze this effect. It is shown that the global increases in vortex decay rate are directly proportional to the magnitude of this highly local relative reaction force.

PACS numbers: 47.55.dd, 47.32.Ef

Keywords: Bubbly Flows, Two-Way Coupling, Euler-Lagrange, Discrete Element Model

[a)]Electronic mail: finnj@engr.orst.edu

[b)]Electronic mail: shamssoe@engr.orst.edu

[c)]Electronic mail: sva@engr.orst.edu (Corresponding Author)

I. INTRODUCTION

The effect of bubbles on surrounding fluid flow is of critical importance in many current research areas such as microbubble drag reduction, cavitation inception, chemical reaction, and small-scale cavitation, among others. In typical operational environments, liquid may be filled with small bubbles which have the potential to modify the flow. As shown by Sridhar and Katz (referred to as S&K in this work)[1], low specific gravity of bubbles entrained in liquids can significantly alter vortical structures as bubbles tend to gravitate toward the vortex centers. Bubble entrainment and interaction with vortical structures has been studied by several groups[2–5], motivated by questions dealing with bubble motion, cavitation, and interphase dynamics. Sridhar & Katz[5] and Van Nierop et al.[3] used experimental techniques to develop models for bubble motion in non-uniform flow, with particular emphasis placed on the determination of the bubble lift coefficient. In a follow-up paper, S&K[1] observed the effects that bubbles, with diameter $400\mu m < d_b < 1,100\mu m$, had on the structure of piston generated vortex rings. Their experimental results show that for a small number of entrained bubbles, at low overall volume fraction, significant distortion of the ring structure was possible under certain conditions. They characterized this distortion by examining sequential PIV images of the bubble entrainment and capture process. In significantly distorted vortices, the presence of the bubbles resulted in a fragmented core, with multiple regions of higher vorticity. Further, the core was shifted upwards, in the direction of the buoyancy force acting on the entrained bubbles. They supplied good analytic rationalization of their results, including the observed vortex distortion at low bubble volume fraction. With proper non-dimensionalization of the bubble equation of motion[6], they derived an independent parameter which was the non dimensional ratio of bubble buoyancy force to hydrodynamic pressure gradient in the vortex. This successfully characterized many of their results, including the bubble *settling locations* or *equilibrium positions*[3].

Modeling approaches for bubbly flows in complex, large scale geometries must be diverse in nature, and capable of handling multiple length and time scales. Direct numerical techniques, capable of fully resolving the interface between the bubbles and surrounding fluid, have been useful for developing lower order models. Oweis *et al.*[2] used front tracking methods to solve the flow field around deforming and cavitating bubbles during entrainment by a Gaussian vortex. Current computational restrictions limit the use of *complete*[7]

models for engineering scale simulations and various levels of approximation must be introduced. Typically, the Eulerian-Eulerian or Eulerian-Lagrangian approach is employed. In an Eulerian-Eulerian or two-fluid model[4,8], both phases are treated as a continuum with unique fluid properties and two sets of Navier Stokes equations are solved. Because the idea of individual particles is not supported, closure models must be used for interphase momentum transfer. In an Eulerian-Lagrangian simulation such as the ones presented in this paper, each bubble is treated as a Lagrangian point-source. Motion of individual bubbles is governed by Newton's second law, and expressions for various forces acting at the centroid of the bubbles are used to advance their position in time. The bubble surface shape is not explicitly represented. With this approach, the effect of the bubbles on the carrier phase are either neglected '*one-way coupling*' or modeled through a reaction source term in the momentum equations '*two-way coupling*'.

For large volume loadings, the volume occupied by the sub-grid bubbles can become considerable, and as they move there can be local variations in bubble volume fraction. Volume averaged equations explicitly accounting for the volume of each individual bubble have been derived[9–11] and commonly used in dense granular flows or fluidized bed studies. In this case, the bubble centroids are still tracked in a Lagrangian frame and the bubble size is assumed smaller than the local control volume. Bubble size is indirectly accounted for by considering the fluid volume displaced. The carrier phase is governed by variable density, zero-Mach number equations and the the liquid flow velocity is no longer divergence free. In addition, the bubbles can influence the fluid through momentum exchange and a reaction force similar to that used in two-way coupling methods. Subsequently, we will refer to this approach as '*volumetric coupling*'. This approach has been used for dense particulate flows[12–16], column reactors[17], and dense bubbly flows[11,18].

In this work, we evaluate the importance of volumetric coupling for bubble-laden flows even under low volume loading conditions. The discrete element approach together with volumetric coupling is used to investigate the effects of bubble entrainment on a traveling vortex tube. To facilitate several parametric studies, we consider a two-dimensional approximation of the vortex ring experiments conducted by S&K[1]. First, it is shown that volumetric coupling effects are necessary to capture the vortex distortions observed experimentally by injecting eight bubbles into the path of a traveling vortex tube. Simulations for this configuration are performed using one-way, two-way and volumetric coupling for

varying strengths of the vortex tube and the diameters of the bubbles. It is shown that, to obtain the trends observed in the experiments related to bubble settling locations and vortex distortions, volumetric displacement effects are important. Second, qualitative and quantitative assessments of the vortex distortion observed in volumetric coupling are made using three methods: bubble induced vortex asymmetry, relative change in the decay rate of angular momentum, and relative change in the peak vorticity. It is found that in all cases the *volumetric* effects result in a relative *increases* in vortex decay rate and peak vorticity.

Figure 1a elaborates the definition of the bubble settling location which is used in understanding many of the results in this work. Imagine that a buoyant bubble is released in the vicinity of a vortex with a core radius, r_c. The magnitude of the fluid angular velocity, u_θ, and vorticity, ω, may vary as functions of radius from the vortex center. Under the right conditions, ie. the vortex is strong enough, the bubble will become entrained in the vortex core. During this process, it may circle the core several times before eventually reaching a settling location with relative coordinates r_s, θ_s measured from the vortex center. At the settling location, there is no motion of the bubble relative to the vortex, meaning that all forces acting on the bubble are in balance. This is shown in figure 1b, where we have included the lift, drag, pressure, added mass, and gravity forces. Note that the pressure force has been split into its dynamic and hydrostatic contributions. For the clockwise vortex shown, the settling location will be in first quadrant of the core where the fluid velocity is turning downward. Mazzitelli & Lohse[19] showed that it is primarily the lift force, which acts perpendicular to the vorticity and slip velocity vectors, that is responsible for bubble accumulation in the downward velocity side of vortices such as this one. This preferential sweeping has been observed in many studies and can lead to bubble clustering, and modulation of turbulence[19–21]. If the flow is steady and axisymmetric then the directionality of the other forces in figure 1b can also be deduced. The net buoyancy force which acts upward is due the addition of the hydrostatic pressure force, $\mathbf{F}_{PH}$ and the bubble weight, $\mathbf{F}_G$. The added-mass and dynamic pressure forces act in the direction of negative dynamic pressure gradient. Neglecting outside disturbances, this will be toward the vortex center. The drag force acts in the direction of the slip velocity vector which, for a stationary bubble in an axisymmetric vortex, is perpendicular to the settling location vector, $\mathbf{r}_s$.

The paper is arranged as follows. In section II, the mathematical formulation of the approach is developed. Next, verification tests on entrainment of a single bubble into a

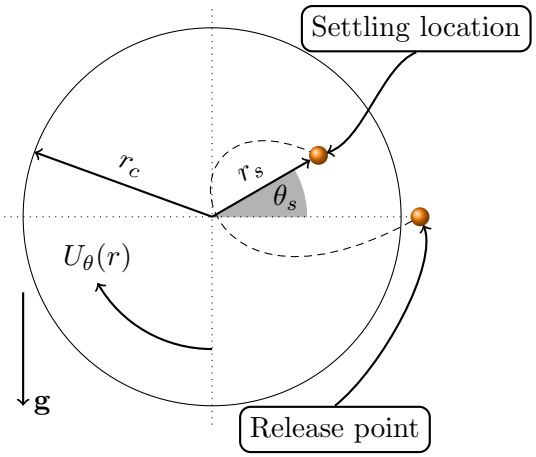

(a)

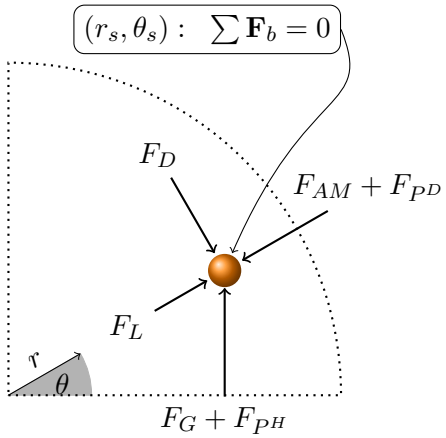

(b)

FIG. 1. Schematic of a bubble entrained in a clockwise vortex and the forces which influence its settling location, (r_s, θ_s).

stationary Gaussian vortex and Rankine vortex are presented in section III. In section IV, eight small bubbles are injected into the path of a traveling vortex tube. Their entrainment, and subsequent interactions with the vortex are compared to the experiments of S&K. Finally, in section V, we examine how the observed large scale changes in vortex decay rate are correlated to the relative intensity of the local bubble-vortex interactions.

II. MATHEMATICAL FORMULATION

The multiphase simulations in this work are carried out using the Eulerian-Lagrangian approach. Here, the motion of the fluid phase is computed using Direct Numerical Simulation

(DNS), and Lagrangian particle tracking is used to solve the motion of the spherical, subgrid scale bubbly phase. Bubble motion in the fluid is calculated from Newton's second law, using expressions for gravity, pressure, lift, drag, and added mass forces. A bubble to fluid reaction is calculated to account for two-way momentum exchange. In addition, in the present formulation, *volumetric* displacement of the fluid by the bubble motion is accounted for by modifying the continuity and momentum equations.

A. Bubble Dynamics

In the Lagrangian reference frame, the equations of motion may be written for each bubble as a system of ordinary differential equations:

$$\frac{d}{dt}(\mathbf{x}_b) = \mathbf{u}_b \tag{1}$$

$$m_b \frac{d}{dt}(\mathbf{u}_b) = \sum \mathbf{F}_b \tag{2}$$

where $\mathbf{F}_b$ is the net force acting on each bubble and has the following contributions:

$$\sum \mathbf{F}_b = \mathbf{F}_G + \mathbf{F}_P + \mathbf{F}_D + \mathbf{F}_L + \mathbf{F}_{AM} \tag{3}$$

The gravitational force, $\mathbf{F}_G$, is the weight of the bubble.

$$\mathbf{F}_G = -\rho_b V_b \mathbf{g} \tag{4}$$

where V_b is the bubble volume and $\mathbf{g} = +9.81 ms^{-2}$ is the gravitational acceleration. The pressure force, $\mathbf{F}_P$, is the force on the bubble due to the total pressure gradient, including the hydrostatic contribution.

$$\mathbf{F}_P = -V_b \nabla P \tag{5}$$

The bubble drag force, $\mathbf{F}_D$ arises due to a difference in bubble and fluid velocities. It is given by:

$$\mathbf{F}_D = -\frac{1}{2} C_D \rho_f A_b |\mathbf{u}_b - \mathbf{u}_{\ell,b}| (\mathbf{u}_b - \mathbf{u}_{\ell,b}) \tag{6}$$

where $A_b = \frac{\pi}{4} d_b^2$ is the frontal area of the bubble and $\mathbf{u}_{\ell,b}$ is fluid velocity interpolated to the bubble location. The bubble slip velocity, $(\mathbf{u}_b - \mathbf{u}_{\ell,b})$ is evaluated using the local velocity field near the bubble of interest. Various empirical expressions have been suggested for the drag coefficient, C_D. For the work on bubble-vortex ring interactions, Sridhar & Katz[5] found that

the drag coefficients were very close to solid sphere drag indicating that the bubble surface was contaminated. In this work, the standard drag curve of Schiller and Nauman[22] for solid sphere drag is used:

$$C_D = \frac{24}{Re_b}(1 + 0.15Re_b^{0.687}) \tag{7}$$

The lift force, F_L, arises for bubbles in shear or rotating flow and has been the subject of much discussion in the literature. In general, it can be expressed as:

$$\mathbf{F}_L = -C_L \rho_\ell V_b (\mathbf{u}_b - \mathbf{u}_{\ell,b}) \times (\nabla \times \mathbf{u}_{\ell,b}) \,, \tag{8}$$

where C_L is the lift coefficient. Various models have been proposed for the lift force[3,5,23,24]. For the bubble-vortex interaction, S&K[5] used the following lift coefficient to obtain the bubble trajectories similar to those observed experimentally[25]:

$$C_L = 0.22\alpha^{-3/4}; \quad \alpha = \frac{|\nabla \times \mathbf{u}_{\ell,b}| d_b}{2|\mathbf{u}_{\ell,b} - \mathbf{u}_b|} \tag{9}$$

The above lift coefficient has significantly higher value than most others; however, it was shown to be necessary to match the bubble trajectories with the experimental data. In the present work, we use the same coefficients. It is shown that, in addition to the above models, to predict the vortex distortion and final settling locations, the volumetric displacement effects are critical.

The added mass force, $\mathbf{F}_{AM}$, is the force which would be exerted on the volume of fluid displaced by the presence of the bubble. It is given by

$$\mathbf{F}_{AM} = \rho_\ell V_b C_{AM} \left(\frac{D\mathbf{u}_{\ell,b}}{Dt} - \frac{D\mathbf{u}_b}{Dt} \right) \tag{10}$$

For small, spherical bubbles, it is generally accepted that $C_{AM} = 0.5$.

The preceding formulation for bubble motion is based on Maxey & Riley's[6] well known equation of motion for a sphere in non-uniform Stokes flow. The effects of higher bubble Reynolds numbers ($\mathcal{O}(100)$), shear induced lift force, $\mathbf{F}_L$ are included in the above formulation. We neglect the Bassett history force, as its value is typically small compared to other forces[5]. Also, we have estimated that for the range of bubble and vortex sizes considered in this study, the contribution of the Faxen force to the overall bubble drag force will be small[26]. For the relatively small bubble sizes considered, we neglect bubble deformation, and assume the bubbles remain rigid spheres. To study larger bubbles with an Euler-Lagrange model, the effects of deformation may be accounted for implicitly by using modified drag

and lift coefficients[27]. Inter-bubble collision forces are neglected in this work due to the low overall volume fraction in the cases studied.

B. Variable Density Fluid Formulation

Consider a domain Γ which contains discrete bubbles dispersed in a continuum fluid as shown in figure 2. Each bubble has a finite, characteristic diameter, d_b, and occupies a volume V_b. The finite size of the bubbly phase may be accounted for by introducing the fluid and dispersed phase volume fractions, Θ_ℓ and Θ_b, where $\Theta_\ell = 1 - \Theta_b$. With proper volume averaging, the conservation equations for mass and momentum of the fluid-bubble mixture become[10,28–30]

$$\frac{\partial}{\partial t}(\rho_\ell \Theta_\ell) + \nabla \cdot (\rho_\ell \Theta_\ell \mathbf{u}) = 0, \tag{11}$$

and

$$\frac{\partial}{\partial t}(\rho_\ell \Theta_\ell \mathbf{u}_\ell) + \nabla \cdot (\rho_\ell \Theta_\ell \mathbf{u}_\ell \mathbf{u}_\ell) = -\nabla P + \nabla \cdot (\Theta_\ell \mu_\ell \mathbf{D}) - \Theta_\ell \rho_\ell \mathbf{g} + \mathbf{f}_{b\to\ell}, \tag{12}$$

where P is the dynamic pressure in the fluid phase, $\mathbf{D} = \nabla \mathbf{u}_\ell + \nabla \mathbf{u}_\ell^{\mathrm{T}}$ is the deformation tensor. Note that no summation is implied on the subscript ℓ. In this form, the fluid velocity field is not *divergence free*, even for an incompressible fluid.

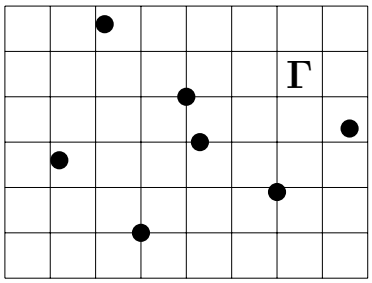

FIG. 2. Illustration of the fluid domain, Γ, containing a subgrid scale dispersed phase.

The reaction force ($\mathbf{f}_{b\to\ell}$) from the bubbles onto the fluid per unit mass of fluid is given as:

$$\mathbf{f}_{b\to\ell}(\mathbf{x}_{cv}) = -\sum_{b=1}^{N_b} \mathcal{G}_\Delta(\mathbf{x}_{cv}, \mathbf{x}_b)(\mathbf{F}_P + \mathbf{F}_D + \mathbf{F}_L + \mathbf{F}_{AM}), \tag{13}$$

where $\mathbf{x}_{cv}$ and $\mathbf{x}_b$ represent the centroids of the control volume (cv) and the bubble, respectively, N_b is the total number of bubbles, and $\mathcal{G}_\Delta$ is an interpolation function from the

bubble locations to the fixed Eulerian grid. Note that the total force on the bubble consists of the pressure force, $F_P = -V_b \nabla P$. The reaction of this force onto the fluid phase results in the force density $+\Theta_b \nabla P$. This reaction term related to the pressure gradient can be combined with the pressure gradient in the momentum equation to obtain:

$$\frac{\partial}{\partial t}\left(\rho_\ell \Theta_\ell \mathbf{u}_\ell\right) + \nabla \cdot \left(\rho_\ell \Theta_\ell \mathbf{u}_\ell \mathbf{u}_\ell\right) = -\nabla P + \nabla \cdot \left(\Theta_\ell \mu_\ell \mathbf{D}\right) - \Theta_\ell \rho_\ell \mathbf{g} + \mathbf{f}'_{b\to\ell} + \underbrace{\Theta_b \nabla P}_{\mathbf{F}_\mathrm{P}\ \text{Force Density}}, \quad (14)$$

where $\Theta_b \nabla P$ is the Eulerian force density obtained from the pressure force and $\mathbf{f}'_{b\to\ell}$ is the Eulerian force density constructed from the Lagrangian force on the bubbles without the pressure force (equation 13 without the pressure force, $\mathbf{F}_P$). Noting that $\Theta_b + \Theta_\ell = 1$, the above equation can be re-written in a more commonly used form by combining the first and last terms on the right-hand side of the above equation[11,30],

$$\frac{\partial}{\partial t}\left(\rho_\ell \Theta_\ell \mathbf{u}_\ell\right) + \nabla \cdot \left(\rho_\ell \Theta_\ell \mathbf{u}_\ell \mathbf{u}_\ell\right) = -\Theta_\ell \nabla P + \nabla \cdot \left(\Theta_\ell \mu_\ell \mathbf{D}\right) - \Theta_\ell \rho_\ell \mathbf{g} + \mathbf{f}'_{b\to\ell}, \quad (15)$$

where $\mathbf{f}'_{b\to\ell}$ contains summation of all reaction forces in equation 13 except the pressure force. This formulation is commonly used in gas-fluidized beds[31,32]. In the absence of any fluid velocity, but in the presence of bubbles, the pressure gradient force is then appropriately balanced by the gravity force.

For large-eddy simulation, the above equations should be spatially filtered using density-weighted Favre averaging[33]. Using the form in equation A.1; however, gives rise to an unclosed term $-\overline{\Theta_\ell \nabla P}$. It is therefore advantageous to use the first form (equation 12), resulting in standard variable density LES equations[34]. In this case, the reaction due to the pressure force is treated *explicitly*. Although in the present study large-eddy simulation is not used, the above form facilitates straightforward implementation of the DEM model in LES framework[3536].

The formulation for the fluid phase given by equations 11, 12, and 13 represents what we will refer to as *volumetric coupling*, where both bubble size and momentum transfer are accounted for. In equations 11 and 12, the point particle approach may be retained by setting $\Theta_\ell = 1$ everywhere. If this is done, the fluid phase is only affected by the bubbles through the source term $\mathbf{f}_{b\to\ell}$ and will be referred to as *two-way coupling*. Additionally, for passive bubbles tracking with *one-way coupling*, the reaction force is also set to zero. Regardless of the coupling model used, the numerical solution of the fluid and bubble motion proceeds in the framework of a fractional step, finite volume solver. Details of the implementation

and numerical algorithm are described elsewhere[35] and are summarized in the Appendix for completeness.

III. VERIFICATION TESTS

Accurate implementation of the various aspects of the DEM model involving bubble tracking, bubble-grid and grid-bubble interpolations and implementation of the reaction forces are first verified through two sets of tests relevant to the present study on bubble-vortex interactions: (i) bubble trajectories in a Gaussian vortex, and (ii) bubble trajectories in a Rankine vortex. The Gaussian vortex case is used to compare the bubble trajectories using one-way coupling with analytical solution. The Rankine vortex case is used to performing error analysis on the reaction force computation using two-way and volumetric coupling. These tests verify that the DEM model and bubble force computations are correctly implemented.

A. Bubble entrainment into a stationary Gaussian vortex

As a first validation case, to show the accuracy of the solver, the entrainment of a single bubble into a stationary Gaussian vortex is considered. The Gaussian vortex is a planar vortex with initial circulation Γ_0 and core radius r_c whose vorticity distribution is a Gaussian function of radius. There is no radial velocity component, and the the tangential velocity can be expressed as follows:

$$u_\theta(r) = \frac{\Gamma_0}{2\pi r}\left(1 - e^{-\eta_1 (r/r_c)^2}\right) \tag{16}$$

The maximum tangential velocity occurs at $r = r_c$ and is given by

$$u_c = \eta_2 \frac{\Gamma_0}{2\pi r_c} \tag{17}$$

where η_1 and η_2 are constants. The vorticity is then:

$$\omega(r) = \frac{\Gamma_0 \eta_1}{\pi r_c^2} e^{-\eta_1 (r/r_c)^2} \tag{18}$$

Assuming axial symmetry, the hydrodynamic pressure gradient is $\partial P/\partial r = \rho u_\theta^2/r$. This flow has been used previously by Oweis et al[2], as a model for wingtip vortices in their study of bubble capture and cavitation inception.

The domain size is approximately $7r_c \times 7r_c \times 0.4r_c$. The no-slip condition is imposed at boundaries in the X and Y directions, and the domain is periodic in the Z direction. The grid is uniform throughout the domain, and uses a spacing of of $\Delta = 1.25mm$. The total number of grid points is $64 \times 64 \times 4$ in the X, Y and Z directions. A total of 14 individual cases of single bubble entrainment, summarized in table I, are simulated using the passive 1-way coupling approach. The velocity field of equation 16 is applied as an initial condition everywhere in the domain, creating a clockwise vortex. A single bubble is released during the first timestep at $r = r_c,\ \theta = 0$. In each case, the fluid velocity and pressure are advanced with a timestep of $\Delta t = 4 \times 10^{-4}s$, while the bubbles are advanced with a smaller timestep of $2 \times 10^{-6}s$ using third-order Runge-Kutta scheme together with sub-cycling[35]. The smaller bubble timestep is dictated by the time-scales associated with different forces on the bubbles and is required to assure that the bubble motion is properly captured. In all cases, gravitational acceleration is $\mathbf{g} = -9.81m/s^2$ in the Y direction, and typical properties of water and air are assumed. Relevant simulation parameters cases are summarized in table II. Bubble diameter, d_b is between 500 and 1300 microns, and initial vortex strengths, Γ_0 is between 0.02 and 0.05 m^2/s. This results in bubble Stokes numbers, $St_b = \overline{\omega} d_b^2/36\nu$, where $\overline{\omega} = \Gamma_0/\pi r_c^2$, which vary from 0.5 and 5.7.

Force balance in the Gaussian vortex:

Since the velocity, vorticity, and pressure gradient are know functions of radius in the Gaussian vortex, it is possible to obtain analytic, coupled expressions for the settling co-ordinates (r_s, θ_s) of entrained bubbles if their motion is governed by the forces outlined in section II. In solid body rotating flow, the vorticity is constant, and tangential velocity varies linearly with radius from the vortex center. Van Nierop et al.[3] used these characteristics along with force balances in the radial and azimuthal directions to develop uncoupled expressions for bubble settling radius and angle in *forced*, rotating flow. Here, we will employ a similar approach to obtain analytic expressions for settling location in the *free*, Gaussian vortex.

Assuming the flow field is steady, and neglecting the Bassett history force, the bubble *settling location* (r_s, θ_s) will be dependent on five forces. These are lift, drag, gravity, added mass, and pressure. Using figure 1b as a guide, a force balance in the azimuthal direction

TABLE I. Parameters for each case of bubble entrainment into a stationary Gaussian vortex.

Case #	$d_b[\mu m]$	$\Gamma_0[m^2/s]$	St_b
1	500	0.03	0.51
2	500	0.04	0.67
3	700	0.02	0.66
4	700	0.03	0.99
5	700	0.04	1.32
6	900	0.03	1.64
7	900	0.04	2.18
8	900	0.05	2.73
9	1,100	0.03	2.45
10	1,100	0.04	3.26
11	1,100	0.05	4.08
12	1,300	0.03	3.42
13	1,300	0.04	4.56
14	1,300	0.05	5.70

TABLE II. Computational parameters used in the setup of the Gaussian vortex case

r_c[mm]	η_1	η_2	Δ[mm]	N_{grid}	Δt[s]	Δt_b[s]
11.45	1.27	0.715	1.25	$64 \times 64 \times 4$	4e-4	2e-6

reveals that the drag force is balanced entirely by a component of the net buoyancy force.

$$(\mathbf{F}_G + \mathbf{F}_{P^H})\cos(\theta_s) = \mathbf{F}_D \tag{19}$$

In the radial direction, there is a balance between the lift force, the dynamic pressure force, the added mass force and a component of the gravity force.

$$\mathbf{F}_B \sin\theta_s + \mathbf{F}_L = \mathbf{F}_{P^D} + \mathbf{F}_{AM} \tag{20}$$

The dynamic pressure force and added mass force can be combined, so that the right hand

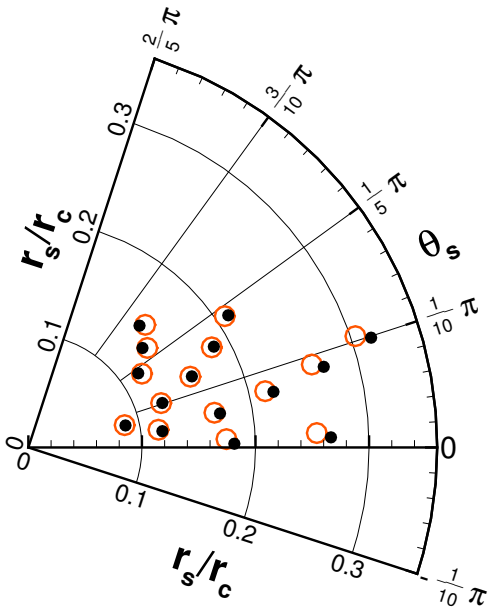

FIG. 3. Settling location of bubbles in the core of the stationary Gaussian vortexes. A comparison of the analytic solution (•) to the solution predicted with the DEM approach (○).

side of equation 20 becomes

$$\mathbf{F}_{P^D} + \mathbf{F}_{AM} = (1 + C_{AM})\,\rho_\ell \frac{u_\theta^2}{r_s} \tag{21}$$

Inserting this and the expressions for $\mathbf{F}_D$, $\mathbf{F}_L$ and $\mathbf{F}_G$ given in section II into equations 19 and 20, the force balances can be rearranged into two coupled equations for r_s and θ_s:

$$\cos(\theta_s) = \frac{3C_D U_\theta^2}{4d_b \mathbf{g}\left[\frac{\rho_b}{\rho_\ell} - 1\right]} \tag{22}$$

$$r_s = \frac{(1 + C_{AM})U_\theta^2}{\left[\frac{\rho_b}{\rho_\ell} - 1\right]\mathbf{g}\sin(\theta_s) + C_L U_\theta \omega} \tag{23}$$

If the flow field inside the vortex core is known (Gaussian, Taylor-Green, Rankine, etc.), and the drag and lift coefficients are specified functions of U_θ and ω, then equations 22 and 23 can be solved iteratively for the bubble settling coordinates. Figure 3 shows a comparison of the settling location predicted by the DEM model with passive, one way coupling, to the values predicted from solving equations 22 and 23 for the 14 individual cases. In the analytic prediction, the value of Γ_0 has been decreased by 12% in all calculations to compensate for the viscous decay which happens before the bubble comes to rest. Time averages of the numerical, 1-way settling location are taken over a period of 0.1 seconds, 1.8 seconds

after injection. The good agreement shows the high accuracy of both the fluid and bubble solutions.

B. Bubble trajectory in a Rankine vortex:

A line vortex (often called Rankine Vortex) is a model for vortical flow generated at the tip of ship propeller blades[37]. The model consists of a forced vortex region in the core of the vortex, and a free vortex region outside the core. Flow velocity and pressure are defined as

$$u_\theta(r) = \left\{ \frac{\Gamma}{2\pi r_c^2} r \, , r \leq r_c; \quad \frac{\Gamma}{2\pi r} \, , r > r_c \right\} \tag{24}$$

$$P_\omega(r) = \left\{ P_\infty - \frac{\rho\Gamma^2}{4\pi^2 r_c^2} + \frac{\rho\Gamma^2 r^2}{8\pi^2 r_c^4}, r \leq r_c; \quad P_\infty - \frac{\rho\Gamma^2}{8\pi^2 r^2}, , r > r_c \right\}, \tag{25}$$

where u_θ is the angular component of velocity vector, $\Gamma = \pi r_c^2 \omega$ is the vortex circulation, ω is vorticity inside the core, r is the radial distance to the vortex center, and r_c is the vortex core radius, within which the circulation is constant, and outside of the core is zero. Vortex core size, vorticity, and circulation which are functions of the velocity in z direction (V_∞) and chord length of the propeller (C_0).

Motion of a single air bubble in a line vortex is simulated using the discrete bubble model with volumetric coupling. This test case shows the ability of the method to accurately predict the bubble motion in a relatively complex flow on an unstructured grid. The flow configuration is the same as medium scale vortex used by[37] and listed in the table III. Bubble

TABLE III. Computational parameters for the Rankine vortex.

Γ (m^2/sec)	V_∞(m/sec)	C_0(m)	r_c(m)	Re_{C_0}	ρ_ℓ(kg/m^3)
1.91511	12.5	0.6096	0.009486	7.62×10^6	1000
Grid Size	small	medium	large		
$N_{xy} \times N_z$	$118^2 \times 3$	$236^2 \times 4$	$472^2 \times 8$		

diameter and density are $d_b = 100$ μm and $\rho_b = 1$ kg/m^3, respectively and it is initially located at $r = 9$ mm from the vortex center.

A cylindrical domain is chosen for this test case. A no slip wall is imposed on the peripheral boundary and a periodic condition on the xy-plane. The computational grid is shown in figure 4. A grid convergence study is conducted by performing simulations at three

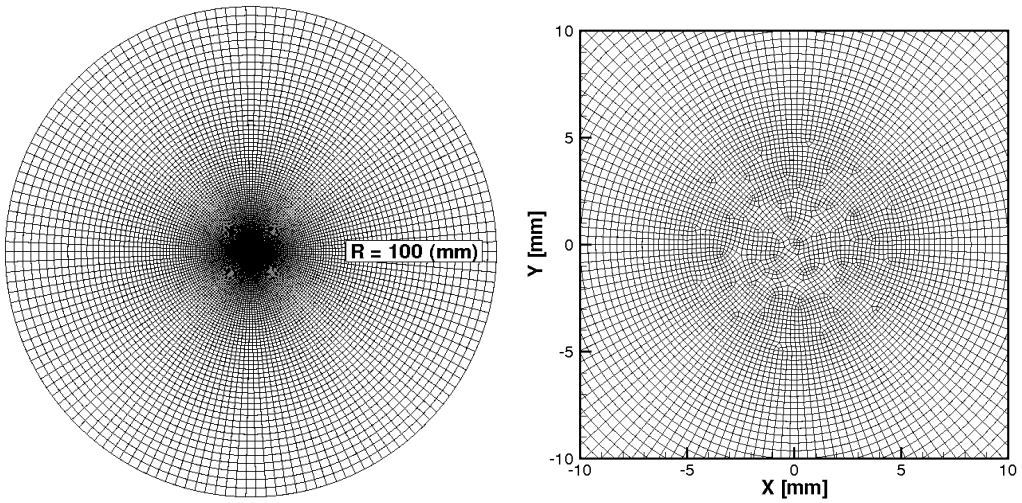

(a)entire domain in vortex plane (b)grid refinement in the vortex core

FIG. 4. Computational grid for the Rankine vortex simulations (coarse grid is shown.)

different resolutions as shown in Table III. The numerical simulation results are compared to the Rankine vortex model to calculate the error associated with the single phase flow itself. Figure 5 shows *L2* norm for error in the horizontal velocity component indicating a second-order accuracy. The error is defined as $u_{error} = |(u_{comp.} - u_{model})|/u_{max}$, where

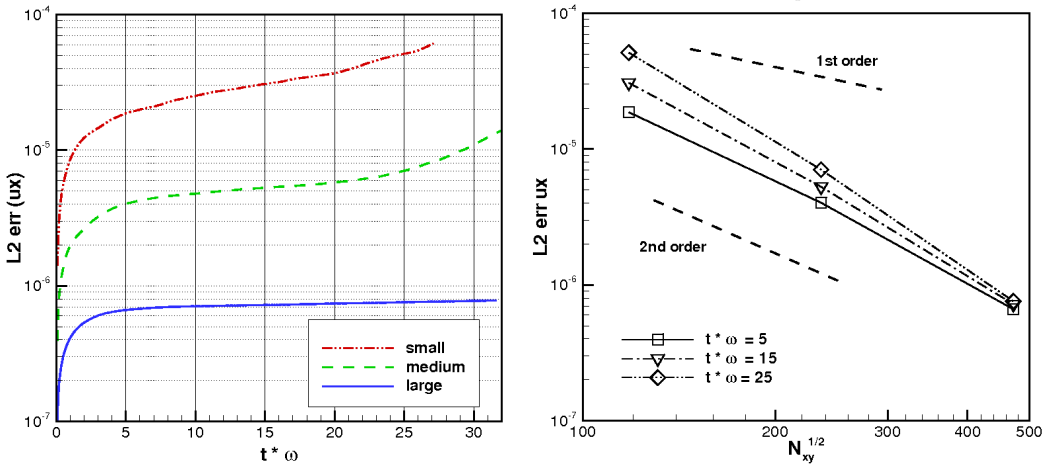

(a)error versus time (b)error versus grid size

FIG. 5. Time evolution of L2 error in the horizontal velocity component for the Rankine vortex.

$u_{comp.}$ and u_{model} are velocity of a particular location from computation and Rankine model, respectively, and u_{max} is maximum velocity in the domain.

The trajectory of a single bubble with 100 μm diameter and density of 1 kg/m^3 is studied in the Rankine vortex. Bubble is initially located close to the vortex edge at $r_0/r_c = 0.95$. The initial velocity is set to the local flow velocity, which is almost the maximum velocity

in the domain. Figure 6 shows the trajectory of the bubble indicating a spiral trajectory towards the vortex center, mainly under the influence of drag, added mass, and pressure forces. The figure compares the trajectory obtained using two approaches for different grid resolutions: (i) the fluid velocity and pressure fields used in the computation of the forces on the bubble (for example, drag, lift, added mass, pressure force etc.) are obtained from the solution of the Navier-Stokes equations, (ii) the fluid and pressure fields are taken from the exact solution of the Rankine vortex (equations 24) at the bubble location.

The first approach includes the interpolation errors from the grid control volume to the bubble location, time and space integration of the fluid flow and the discrete bubble equations. The latter approach basically provides the true trajectory of the bubble if the effect of the bubble motion on the fluid flow is neglected. For a large section of the bubble trajectory, all three grid resolutions show very close agreement with the direct integration result. Near the vortex center; however, the coarse grid is less accurate, due to insufficient grid resolution (shown in figure 6(b)).

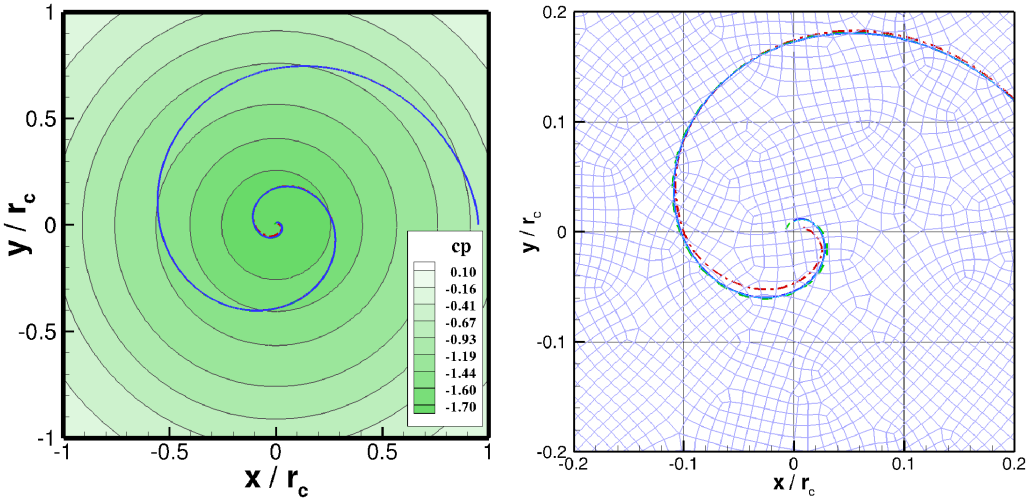

(a)C_p contours and trajectory (b)medium grid shown

FIG. 6. Trajectory of single bubble using small (dash-dotted red line), medium (dashed green line), and large (solid blue line), in comparison to the results from direct integration of equations of motion in Rankine vortex model (solid cyan line).

In order to further quantify the accuracy of the bubble trajectory, an L2 error in trajectory is monitored (figure 7). Here the error is defined as $r_{err} = |(r_{comp} - r_{dirint})|/r_c$, where r_{comp}, and r_{dirint} are bubble distance to the vortex center from the computation and direct integration, and r_c is the vortex core radius. The error is integrated in time to calculate the

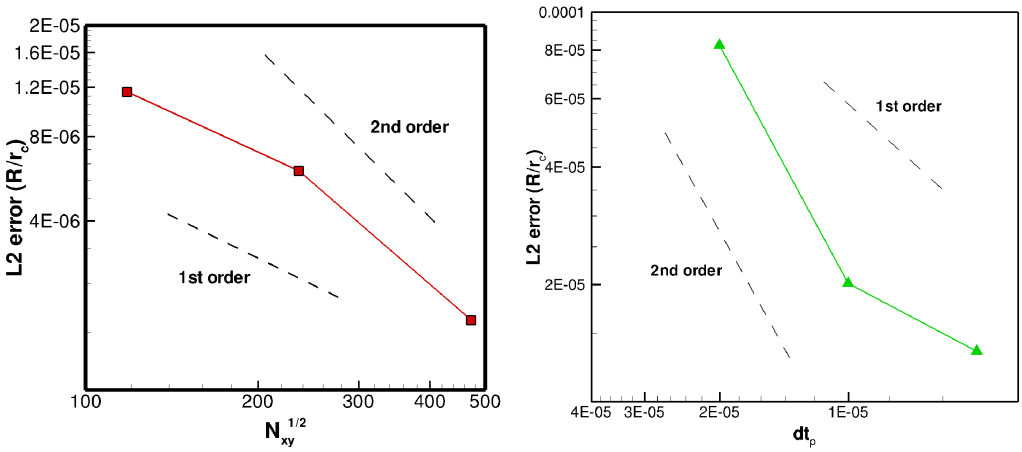

(a)L2 error for different number of grids (b)L2 error for different time steps

FIG. 7. Error in the trajectory of a single non-cavitating bubble in a Rankine vortex,

L2 norm. Close to second order convergence is observed.

IV. BUBBLE INTERACTIONS WITH A TRAVELING VORTEX

Interactions of few small bubbles with a traveling vortex are studied in detail using the one-way, two-way, and volumetric coupling. The traveling vortex is obtained from a pulsed jet with flow conditions based on the experiments by Sridhar & Katz[1] on traveling vortex ring.

A. Vortex Tube Generation

In this section, the interactions of eight small bubbles with a jet generated, traveling vortex tube are studied. The intention is to compare results with the experiments of Sridhar & Katz[1]. Although the present study is two-dimensional in nature (vortex tube) in contrast to the fully three-dimensional experiment (vortex ring), care has been taken to assure that the setup and parameter space will permit a good degree of comparison. The domain considered is shown in Figure 8. The total domain size is 10 h_{jet} in X by 3 h_{jet} in Y and is centered at $Y/h_{jet} = 0$, where h_{jet} is the height of the inlet jet used to generate the vortex tube. At the left wall, the no-slip condition is enforced for $|Y| \geq h_{jet}/2$ when the inlet jet is active, and for all values of Y after the inflow jet is shut off. The entire right hand boundary is treated as a convective outlet. No-slip walls are enforced at $Y/h_{jet} = \pm 1.5$. The

two-dimensional domain is periodic in the Z direction, with a thickness of $L_z = h_{jet}/20$.

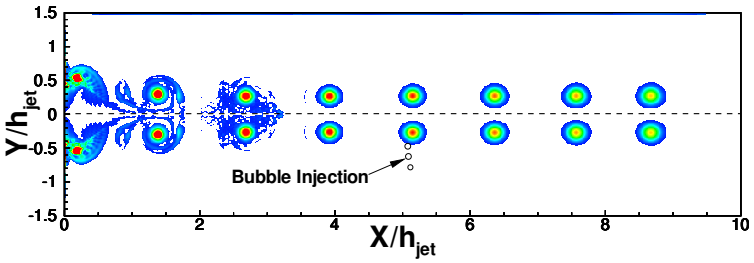

FIG. 8. Two, symmetric vortex tubes are created by an inlet jet pulsed at X=0. Contours show vorticity out of the plane during vortex roll-up and advection downstream.

At the inlet boundary, a jet is pulsed for 0.27 seconds into the initially quiescent domain which causes the roll up of two symmetric vortex tubes as shown. The jet inflow velocity is a function of time, and is described by a polynomial, with coefficients summarized in table IV. Figure 9 compares the shape of a simulated inlet velocity pulse to one used by S&K to generate an experimental vortex ring. The shape of experimental pulse is well represented by the simulated inflow, and the resulting vortex tubes are comparable in size and strength to cross sections of the experimental vortex rings. The inlet is modeled as an orifice rather than the piston/nozzle assembly used in the experiments. It was shown by James & Madina[38] in a study of vortex ring formation that the difference between the two inlet types for laminar vortex rings is small. Three different vortex strengths are obtained by scaling the velocity profile shown in figure 9 by 1.0, 1.3, or 1.6. The strength is characterized by the initial circulation of the vortex tube and can calculated from the inlet velocity profile as

$$\Gamma_0 = \int_0^T \frac{U_0^2(t)}{2} dt = 159;\ 207;\ 254\ cm^2/s \tag{26}$$

The vortex Reynolds number for these vortices is calculated based on the cylindrical slug model of Glezer[39]

$$Re_{vx} = \frac{1}{2\nu} \int_0^T U_0^2(t) dt = 15900,\ \ 20700,\ \ 25400 \tag{27}$$

Glezer[39] characterized the transition from laminar to turbulent vortex rings based on the ring strength and generator piston aspect ratio (L_p/D_p). For the present vortex tube Reynolds numbers, a corresponding vortex ring in 3D would exceed the turbulent transition line for the piston stroke aspect ratio used by S&K. Indeed, the present vortex tube shows some

turbulent characteristics during the roll-up phase, but in two dimensions they remain mostly stable and laminar as they travel downstream to the point of bubble injection.

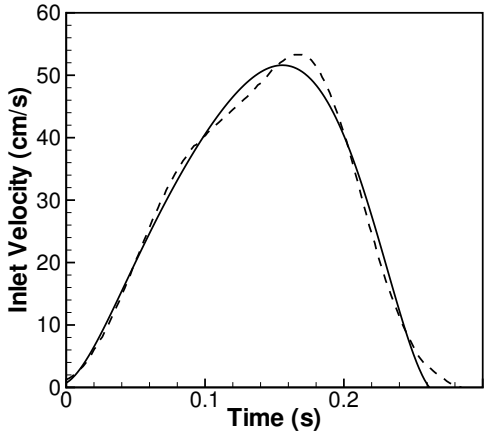

FIG. 9. Prescribed inlet velocity (—), based on S&K[1] (– – –)

To reduce computational expense, a plane of symmetry is assumed at $Y/h_{jet} = 0$, where a free slip condition is imposed ($\partial \mathbf{u}/\partial \hat{\mathbf{n}} = 0$), and only the bottom vortex tube shown in figure 8 is considered. A uniform Cartesian grid is used throughout the area below the line of symmetry with a total of $800 \times 121 \times 4$ elements in the X, Y, and Z directions. This results in a grid spacing of $\frac{h_{jet}}{\Delta} = 80$. Once stable, the vortex core diameter is resolved by approximately 20 grid points per diameter. Computational parameters relevant to the domain and vortex generation are summarized in table IV.

TABLE IV. Computational parameters for the vortex tube case

Parameter	Value
ρ_ℓ	1,000 kg/m^3
ν_ℓ	1e-6 m^2/s
Domain Size	1m x 0.15m x 0.005m
Grid Size	800 x 121 x 4
Jet height (h_{jet})	0.1 m
Inflow time	0.27 s
Inflow Velocity	$U(t) = C \cdot \sum_{i=1}^{7} a_i t^{7-i}$; $a_1 = 62,278$, $a_2 = -47,082$, $a_3 = 13,686$, $a_4 = -2062$, $a_5 = 159.5$, $a_6 = -1.289$, $a_7 = 0.006$; $C = 1.0,\ 1.3,\ 1.6$

After the jet is pulsed, the shear layer rolls up into a vortex tube. The contours in figure 8 show the diffusion of the high vorticity in the core as the vortex tube travels downstream. At each timestep, the core center is located by determining the centroid of vorticity, defined as (following S&K):

$$X_c = \sum_i X_i \omega_i^2 \Big/ \sum_i \omega_i^2 \qquad Y_c = \sum_i Y_i \omega_i^2 \Big/ \sum_i \omega_i^2 \tag{28}$$

where ω_i is the local vorticity at the coordinates (X_i, Y_i). The motion of the computed centroid is shown in figure 10 up to the point of bubble injection. Oscillations in the Y direction stabilize after $X/h_{jet} = 2$, once the vortex has rolled up completely. The core remains nearly axisymmetric in shape, and the center travels along the line $Y/h_{jet} = -0.27$ with a convective velocity of approximately 14% of the maximum inlet velocity.

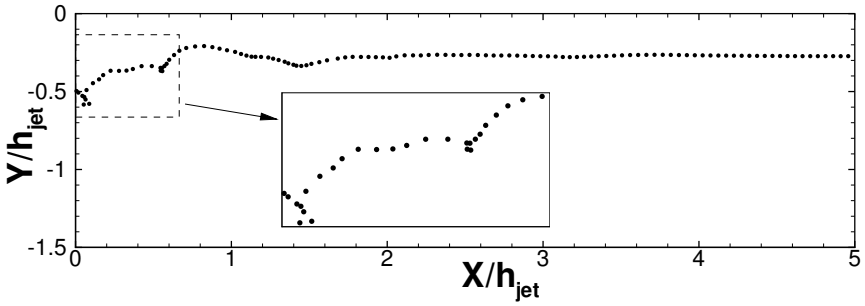

FIG. 10. Vortex core trajectory tracked by following the center of vorticity.

In addition to examining the contours of vorticity, the instantaneous shape of the vortex core may be visualized by creating radial and azimuthal mappings of the core vorticity distribution. This technique will later be used to quantify the vortex distortion caused by entrained bubbles in section IV D. At selected intervals, the vorticity distribution is mapped onto a cylindrical coordinate system centered at X_c, Y_c. This is accomplished using a discrete averaging procedure that includes each grid point within the core radius. Figure 11 shows the results of this technique applied to the initial, asymmetric stages of vortex formation ($X/h_{jet} \approx 0.1$), and to the fully developed stage ($X/h_{jet} \approx 5$). In the initial stage, the azimuthal vorticity distribution (figure 11(a)) shows the irregular shape of the core. The radial vorticity distribution (figure 11(b)) shows that there is a high gradient of vorticity in the radial direction, that has yet to diffuse. At much later times, the vortex is stable and the core is nearly axisymmetric in shape (figure 11(c)). Again, the azimuthal mapping

scheme captures this accurately. The fully developed radial distribution (figure 11(d)) shows that the core has approached a Gaussian distribution of vorticity. Indeed, a comparison of the traveling vortex tube and the stationary Gaussian vortex from section III A, made in figure 12, shows the flow structures are very similar. The vorticity contours show that the traveling vortex tube is elongated slightly in the axis of vortex motion, while the Gaussian vortex is perfectly symmetric. However, the differences in the average radial vorticity distribution of the two vortices are very small, which suggests that the extension of the Gaussian model to the analysis of this case is appropriate. In[5] and[1], S&K have assumed a constant core radius of 1cm across all cases. We will also assume the radius is constant but instead use the Gaussian vortex radius, r_c, meaning that the vortex radius is the radius of maximum angular velocity. Across all three vortex strengths, this radius is equal to $r_c = 1.145\ cm$, and varies only slightly as the vortex travels downstream.

B. Bubble injection

Once the vortex reaches a downstream position of $X/h_{jet} = 5.0$, eight bubbles are injected below and in front of the vortex core. The bubbles are injected, one at a time, with a time of $\Delta t_{inj} = 10ms$ between injections. Due to buoyancy, the bubbles rise and are entrained into the vortex core. The injection point moves downstream with the vortex, so that it is stationary with respect to the vortex core. This is illustrated in figure 13. Despite unique release points and times, the bubbles all follow a similar trajectory in the cylindrical reference frame which moves with the core. A parametric study is performed to determine the effects of bubble size and vortex strength on settling location and vortex distortion. The bubble diameter, d_b, and vortex strength, Γ_0, are varied over a similar range as in the experiments of S&K. The parameters associated with 12 individual cases are summarized in table V. The non-dimensional parameter $(\mathbf{g}d_b)/(8\Gamma_0^2)$ ranges from 7×10^{-8} to 2.61×10^{-6}. The bubble Stokes number has values between 0.27 and 2.07. Gravity is fixed at $g = 9.81\ m/s^2$. Each case is simulated using the three approaches outlined in the introduction; (i) the passive one-way coupling approach, (ii) the point-particle two way coupling approach, and (iii) the finite size volumetric coupling approach.

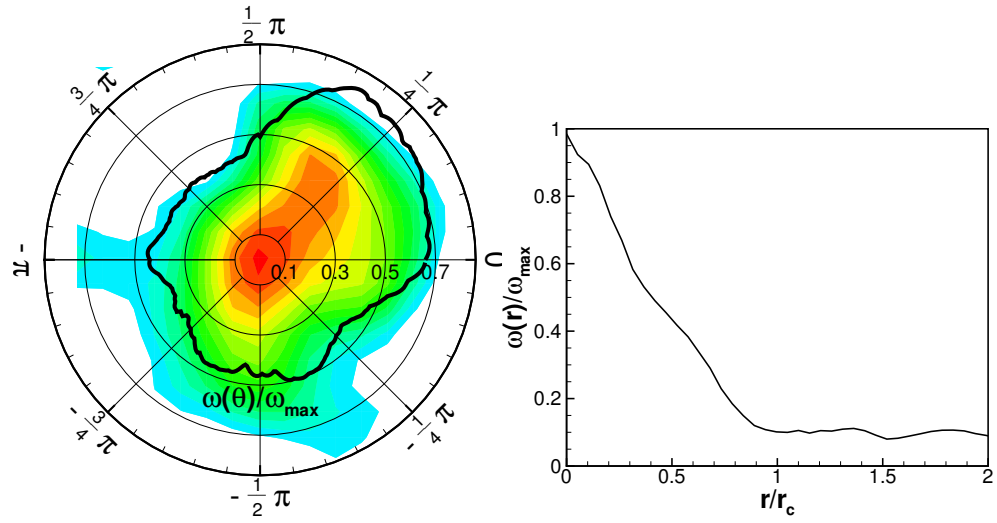

(a) (b)

Initially asymmetric core during vortex roll up

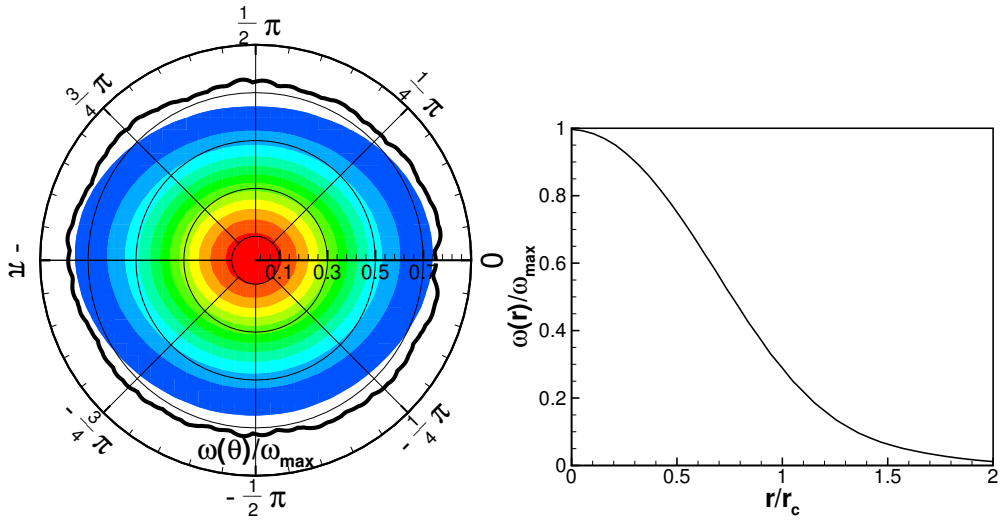

(c) (d)

Fully developed, nearly axisymmetric, Gaussian core at $X/h_{jet} = 5$

FIG. 11. Discrete mapping of the vortex core shape into a cylindrical reference frame which moves with the core. Left panel figures (a & c) are contours of vorticity overlaid with the azimuthal vorticity distribution. Right panel figures (b & d) are the radial vorticity distributions. Vorticity is normalized by the maximum core vorticity, ω_{max}.

C. Bubble trajectory and settling location

The first result of interest is how bubble trajectory during entrainment changes with bubble size and vortex strength. In all cases, each of the eight bubbles are entrained by the

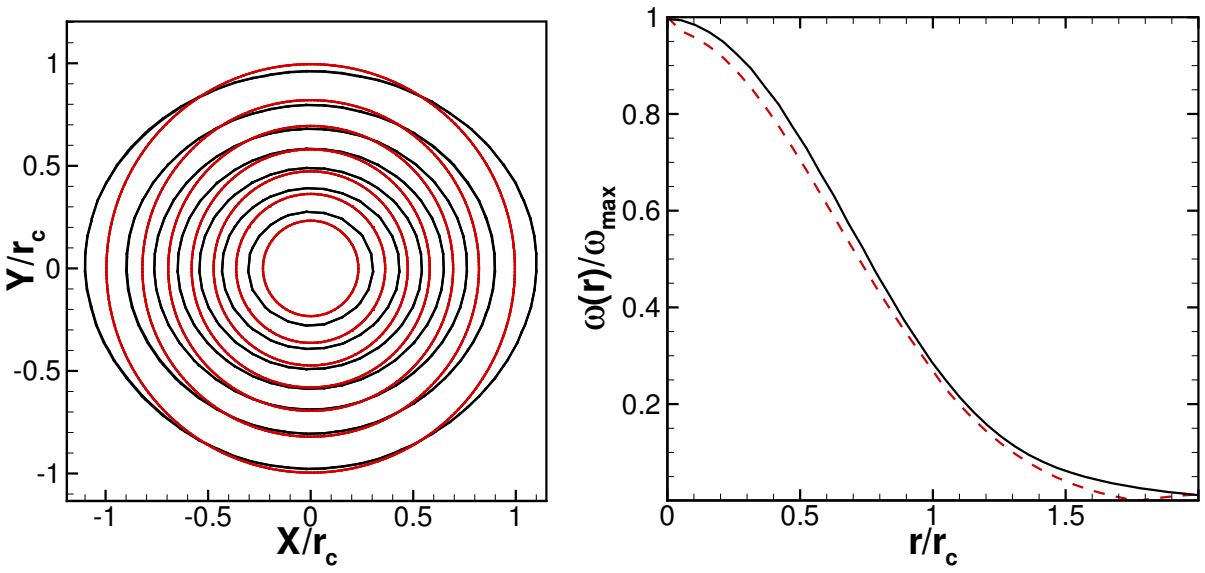

(a) (b)

FIG. 12. (a) Comparison of the out of plane core vorticity normalized by ω_{max} in the traveling vortex tube (—) and the stationary Gaussian vortex (—). (b) Comparison of radial distribution of vorticity in the traveling vortex tube (—) and the stationary Gaussian vortex (- - -)

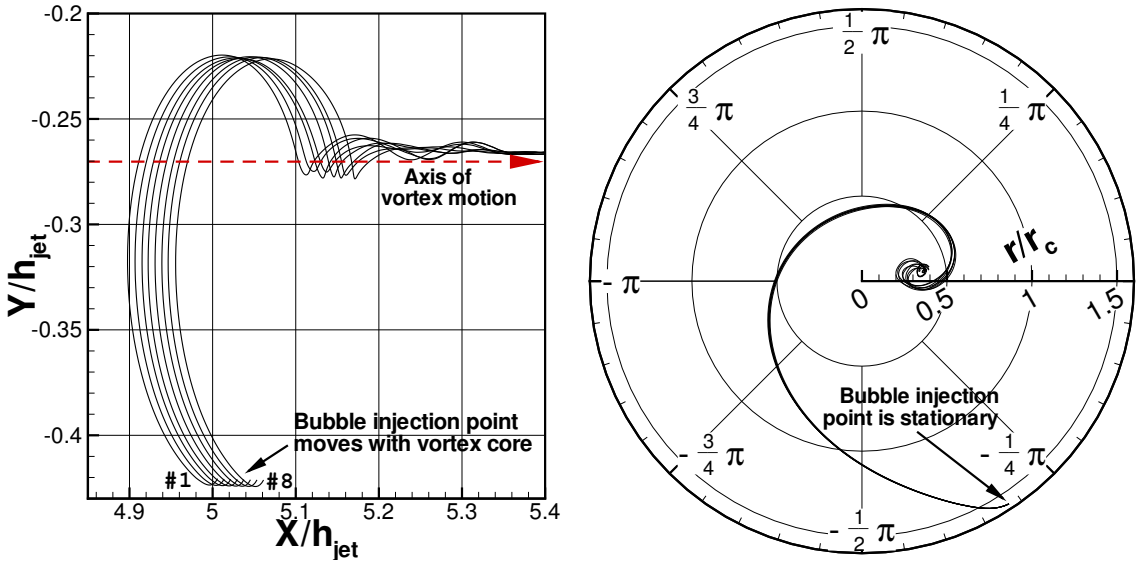

(a)Stationary Cartesian frame (b)Moving Cylindrical frame

FIG. 13. Release points and trajectories of eight bubbles from case #10 in (a) a stationary, Cartesian frame of reference (b) a cylindrical reference frame which moves with the vortex center.

TABLE V. Summary of vortex tube parametric study

Case	$d_b[\mu m]$	$\Gamma_0[m^2/s]$	St_b	$\frac{\mathbf{g}d_b^3}{8\Gamma_0^2}(\times 10^6)$
#1	500	0.0159	0.27	0.61
#2	500	0.0207	0.35	0.36
#3	500	0.0254	0.43	0.24
#4	700	0.0159	0.53	1.66
#5	700	0.0207	0.68	0.98
#6	700	0.0257	0.84	0.65
#7	900	0.0159	0.87	3.54
#8	900	0.0207	1.13	2.09
#9	900	0.0254	1.39	1.39
#10	1,100	0.0159	1.30	6.46
#11	1,100	0.0207	1.69	3.81
#12	1,100	0.0254	2.07	2.53

passing vortex tube. They rise from their release point around the rear of the vortex and are swept into the downward velocity region on the forward side of the core. The Stokes number is the parameter which has the greatest effect on the trajectory during the entrainment process. Figure 14 shows the effects of increasing Stokes number on the trajectory of bubbles in cases 1, 4, 7, and 10 during entrainment. For these cases, the initial vortex strength is fixed at $\Gamma_0 = 0.0159\ m^2/s$ and Stokes number varies due to changes in bubble size. In case #1, the bubble Stokes number is small, and the bubble follows the fluid streamlines closely as it spirals towards the core. With increasing Stokes number, this spiral becomes tighter and the bubble takes a more direct path to the settling location. For a fixed vortex strength, the settling radius increases with bubble diameter due to increases in both buoyancy and lift forces.

At the settling location, the bubbles do not remain perfectly stationary because of local flow variations, but in the mean, their position is steady. In order to account for these slight variations, the settling coordinates of each case are averaged for all bubbles over a distance of $5.2X/h_{jet} < X_{vx} < 5.9X/h_{jet}$. Table VI lists these results for each coupling model. The point-particle, two-way coupling approach results in less than 1% difference in settling loca-

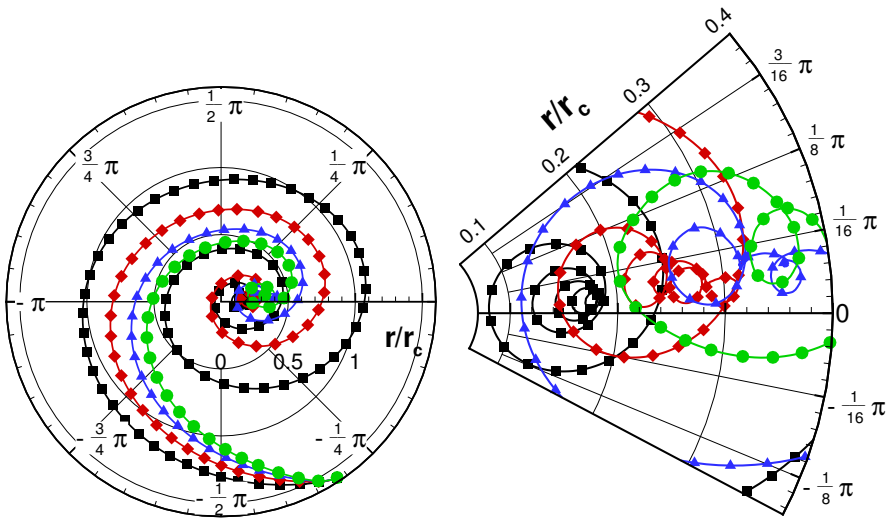

(a)Bubble release and entrainment (b)approaching the settling location

FIG. 14. Effects of increasing bubble size on the entrainment trajectory and settling location in the traveling vortex. A single trajectory is shown for one of 8 bubbles being entrained into a vortex of strength $\Gamma_0 = 0.0159 m^2 s^{-1}$. ■ $500 \mu m$ (case #1), ♦ 700 μm (case#4), ▲ 900 μm (case #7), ● 1100 μm (case #10). All results shown use the volumetric coupling approach.

tion across all cases when compared to the passive one-way coupling model, indicating that the two-way coupling term $\mathbf{f}_{b\to\ell}$ is not significant at these low volume/mass loadings. The settling locations for the two-way and volumetric coupling approaches are plotted against the non-dimensional parameter $\mathbf{g}d_b^3/8\Gamma_0^2$ in figure 15 alongside the experimental data of S&K. Care has been taken to normalize the data in a consistent manner to the experiments. Excellent agreement is obtained with the volumetric coupling approach over the entire range of present conditions, while the two-way coupling approach shows considerable scatter and a consistently smaller settling radius than the experiments. This indicates that the disturbed flow field generated due to *local* variations in the bubble volume fraction accounted in the volumetric coupling approach is critical to predict the settling location correctly for even small bubbles. Further, this shows that the strong lift coefficient measured by S&K *must* be used with a volumetric coupling approach for correct predictions.

TABLE VI. Results of bubble settling location. Angles are listed in radians

	Settling coordinates $\left(\frac{r_s}{r_c}, \theta_s\right)$	
Case	One-way & Two-way Coupling	Volumetric Coupling
#1	0.18, 0.13	0.19, 0.11
#2	0.10, 0.21	0.11, 0.27
#3	0.08, 0.35	0.08, 0.32
#4	0.21, 0.16	0.26, 0.16
#5	0.14, 0.31	0.18, 0.22
#6	0.11, 0.48	0.13, 0.36
#7	0.27, 0.21	0.36, 0.12
#8	0.18, 0.39	0.26, 0.24
#9	0.13, 0.59	0.20,0.38
#10	0.32, 0.25	0.46, 0.11
#11	0.22, 0.46	0.33, 0.23
#12	0.15, 0.70	0.27, 0.46

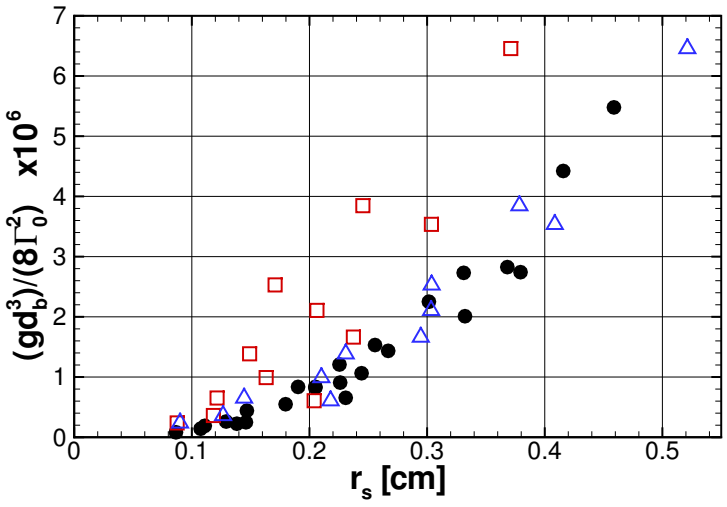

FIG. 15. Comparison of the non-dimensional settling location with the experimental results of Sridhar & Katz. The parameter $gd_b^3/8\Gamma_0^2$ is the non-dimensional ratio of the buoyancy force and the hydrodynamic pressure gradient experienced by the bubble. ● Experimental data, □ one-way & two-way coupling results, △ volumetric coupling.

D. Vortex distortion

Knowing that the volumetric coupling approach can accurately predict the entrainment and settling locations of the eight bubbles into the vortex core, we now investigate the effects that the bubbles have on the vortex structure after entrainment. The vortex cores of cases #1, #7, and #10 are visualized in figure 16, at approximately the same location, 8 cm downstream of the bubble injection point. Contours of vorticity are shown for each case together with a plot for the case with no bubbles for comparison (figure 16(a)). The instantaneous radial vorticity distribution corresponding to each of these contour plots is shown in figure 17. Together, these two results illustrate the progression from negligible to significant vortex distortion in range of cases studied. The undistorted vortex from case #1 is shown in figure 16(b). Here, the contours of vorticity remain mostly symmetric about the $\theta = 0$ and $\theta = \pi/2$ planes, with a slight elongation in the flow direction. The corresponding radial vorticity distribution in figure 17(b) shows that the Gaussian profile is retained. The inner core experiences a slight drop in vorticity, and there is a small average increase in vorticity between about $r/r_c = 0.3$ to 0.4. At greater distance from the vortex center, the Gaussian vortex profile is quickly recovered, and there is little change compared to the case with no bubbles injected. More noticeable changes to the flow structure are observed in case #7, shown in figures 16(c) and 17(c). The presence of the bubbles has resulted in a noticeable but relative small asymmetry in the inner core ($r/r_c < 0.5$). In particular, a band of higher vorticity is created, with the largest values located just outside the settling radius of the bubbles. There is a corresponding decrease in the strength of the inner core, and the radius of maximum average vorticity is shifted outward from the center. A significantly distorted vortex from case #10 is shown in figures 16(d) and 17(d). Again, the bubbles result in a band of higher average vorticity just outside the settling location. The core has become highly asymmetric and unstable due to the presence of the larger, 1100 μm bubbles. The Gaussian profile of radial vorticity is essentially destroyed for $r < r_c$, and a strong peak vorticity is observed near $r/r_c = 0.6$.

In their experimental work, S&K characterized the vortex distortion by calculating the shift in the vorticity centroid, (X_{vx}, Y_{vx}) as well as the change in peak vorticity in the core. In highly distorted cases, the core was shifted upward during the entrainment process and fragmented into several regions of increased vorticity. In the present computations, the shift

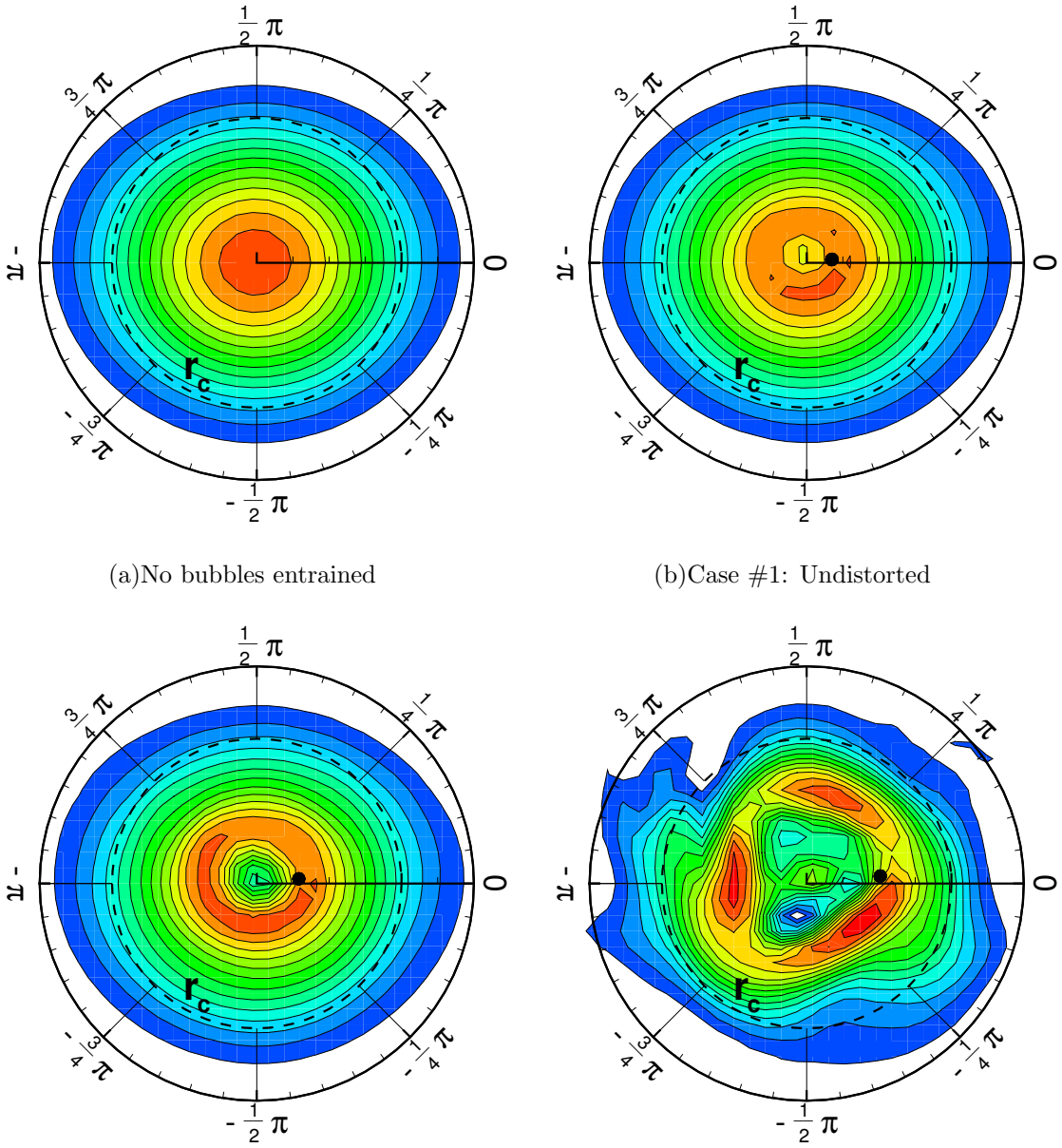

(a)No bubbles entrained

(b)Case #1: Undistorted

(c)Case #7: Marginal distortion

(d)Case #10: Significant distortion

FIG. 16. Contours of out of plane vorticity in the vortex core with initial strength $\Gamma_0 = 0.0159\ m^2/s$ at a location 8cm after bubble injection. The ● indicates the average settling location of the 8 entrained bubbles. Vortex motion is from left to right.

of the vorticity centroid is not a reliable indicator of observed distortion magnitude, perhaps due to the periodic, two-dimensionality of the flow. Instead, we choose to assess the vortex distortion both qualitatively and quantitatively using three measures. The results for all cases are summaraized in table VII. First, we observe the degree to which the vortex core

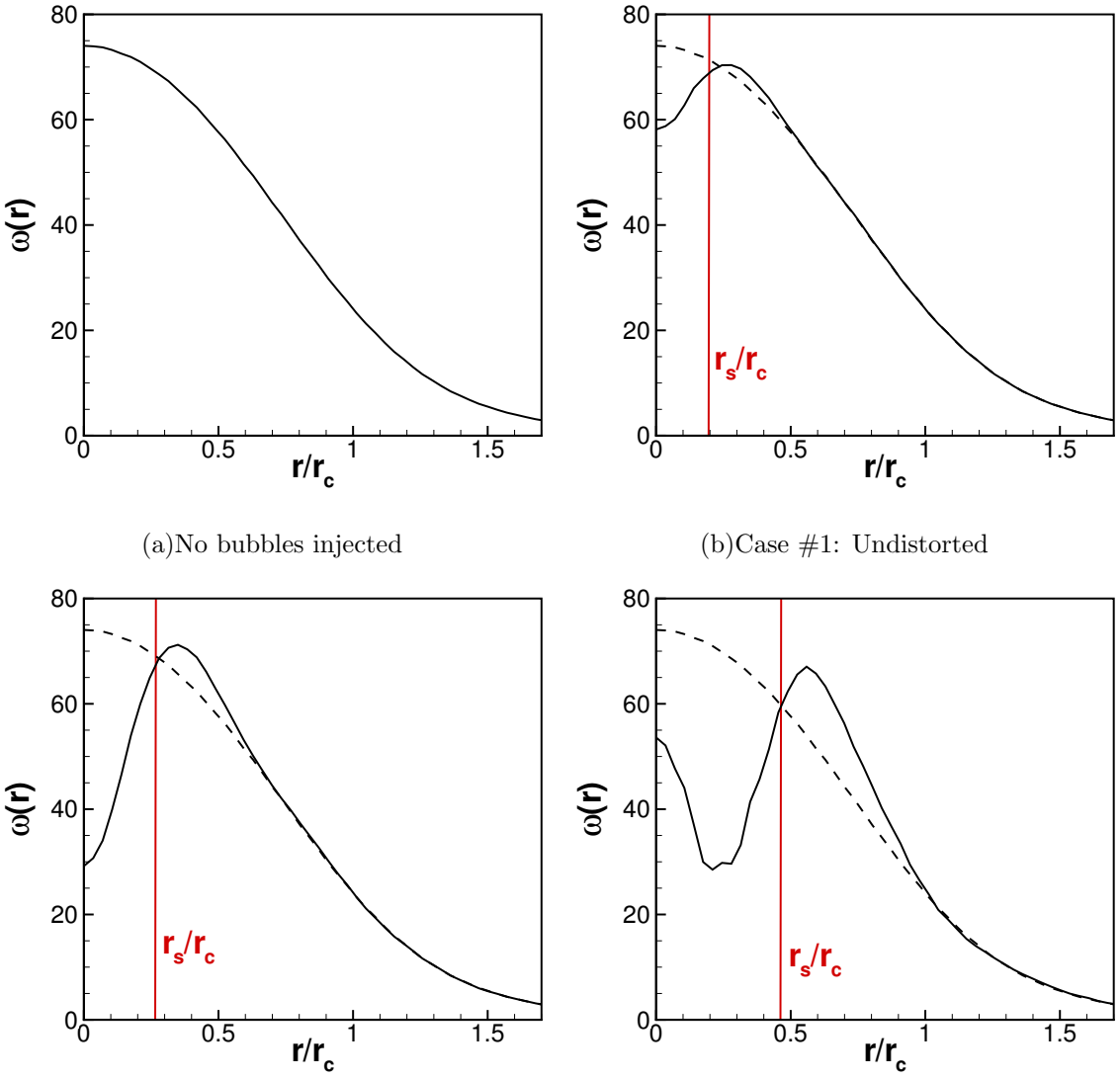

(a)No bubbles injected

(b)Case #1: Undistorted

(c)Case #7: Marginal distortion

(d)Case #10: Significant distortion

FIG. 17. Radial vorticity distributions corresponding to the vortex cores in figure 16. (—) volumetric coupling; (- - -) one-way coupling results. Solid red lines correspond to the average bubble settling radius. These radial profiles are obtained by averaging in the azimuthal direction.

is fragmented or becomes asymmetric during the simulation. This is an entirely qualitative assessment, but is an important contribution of the volumetric coupling model. Second, we calculate the time averaged increase of peak vorticity, ω_p, in the vortex core. This is a straightforward, quantitative measure which can be used to compare to S&K's experiment. They observed that in distorted vortices, the peak measured vorticity in the core increased up to 28%. In the present study, we have calculated the increase as:

$$\text{Relative increase in max vorticity } (\%) \ = W = \frac{\overline{\hat{\omega}_p - \omega_p}}{\omega_p} \times 100, \tag{29}$$

where ω_p and $\hat{\omega}_p$ are the instantaneous peak vorticity values observed for passive (1-way coupling) bubbles and bubbles modeled with volumetric coupling, respectively. The overbar indicates averaging in the time it takes for the vortex core to travel from $X = 5.2h_{jet}$ to $X = 5.8h_{jet}$. In the present results, the values of W range from almost zero for case #3 to 39% in case#12, a similar range as in S&K's experiments. Third, and most importantly, we calculate the change in the decay rate of angular momentum due to volumetric coupling. This calculation is illustrated in figure 18. The instantaneous angular momentum in the core is calculated by summing the momentum of all control volumes in the core

$$L_{vx} = \sum_{\text{core cv's}} \rho_\ell U_\theta r_{cv} V_{cv} \tag{30}$$

Where r_{cv} is the distance from the vortex centroid to the *cv* center and V_{cv} is the *cv* volume. The decay rate is then just the time derivative of the angular momentum.

$$\text{Decay rate} = \epsilon = \frac{d(L_{vx})}{dt} \tag{31}$$

In *all* cases, we observe an increase of the decay rate from ϵ to $\hat{\epsilon}$ when considering volumetric coupling, although the relative amount of this increase varies significantly. To normalize the amount across all cases, we introduce the relative change in decay rate,

$$\text{Relative change in decay rate } (\%) = E = \frac{\overline{\hat{\epsilon} - \epsilon}}{\overline{\epsilon}} \times 100 \tag{32}$$

Again, the overbar denotes the average decay rate measured between $X = 5.2h_{jet}$ to $X = 5.8h_{jet}$. Together these three criteria evaluate the bubble induced vortex asymmetry, the local volumetric effects (W), and the more global volumetric effects (E).

Table VII contains a significant amount of information, and so we will attempt to extract from it some consistent trends. It is observed across all cases that the effect of the finite size of bubbles modeled through volumetric coupling is to decrease the vorticity at a radius inside the bubble settling location, and increase the vorticity in a band outside of settling location. This core topology change causes both an *increase* in the maximum vorticity by a factor W and an *increase* in the decay rate by a factor E. It will be shown in the next section that this increased decay rate scales linearly with the relative magnitude of the local bubble-vortex interactions. In their experimental results, S&K seemed to observe more frequent and distinct fragmenting of the core into multiple regions of high vorticity. In this study, the only case to exhibit significant and consistent core fragmentation is case

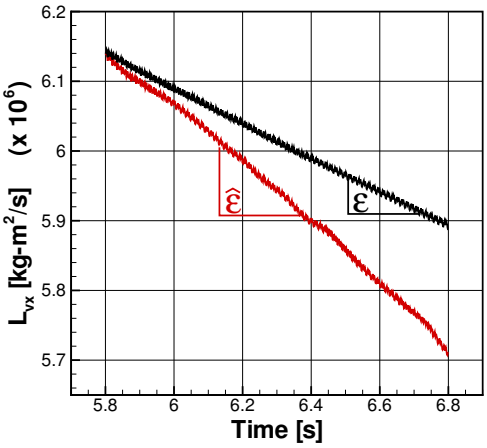

FIG. 18. Illustration of the characteristic increase of angular momentum decay rate when volumetric coupling is used. L_{vx} is the instantaneous vortex angular momentum. (—) Passive, 1-way bubbles, ϵ is the decay rate. (—)Volumetric coupling, $\hat{\epsilon}$ is the decay rate.

TABLE VII. Observed and calculated vortex distortion measures.

Case	Core Fragmentation & Asymmetry	W	E
#1	None	0.57%	4.37%
#2	None	0.01%	2.18%
#3	None	0.00%	1.31%
#4	Some	3.01%	20.17%
#5	Some	2.28%	10.34%
#6	None	0.62%	5.47%
#7	Some	6.72%	60.27%
#8	Some	7.92%	30.69%
#9	None	10.0%	18.08%
#10	Significant	14.84%	144.70%
#11	Some	17.90%	70.91%
#12	Some	39.02%	46.63%

#10, shown in figure 16(d). This case is the combination of the largest bubble size, and the weakest vortex. These conditions allow the bubbles to settle farther away from the center, at $r_s/r_c = 0.46$. Here, the bubble Reynolds number based on the undisturbed flow field is 124. Because the bubbles in this study are subgrid in size, we cannot infer too much about

the mechanisms of bubble-fluid interaction which lead to the creation of instability and the high vorticity band. We know however, that wake effects and unsteadiness are amplified as the bubble Reynolds number is increased, that is, when the bubble size or flow velocity is increased. This explains why smaller bubbles which settle closer to the vortex center result in less significant vortex distortion. Preliminary results from a complimentary, fully resolved study of a bubble entrained in a stationary, 2D, Gaussian vortex patch indicate that the wake behind the bubble causes significant increases in local vorticity magnitude[40].

Although S&K were concerned only with a two dimensional slice of their vortex rings, their flow was inherently three dimensional. Application of our present methods to the three-dimensional vortex ring problem is mostly straightforward. Such a simulation would allow a more direct comparison with the experimental results and should be pursued in the future. However, in the present work a two-dimensional approximation was introduced to facilitate several parametric studies varying bubble size and vortex strength. Even for the vortex ring experiments, S&K observed that the bubbles remained in a single plane at the bottom of the ring, suggesting that a two-dimensional simulation may be a reasonable approximation. The transport equation for vorticity in an incompressible fluid with constant properties is

$$\frac{D\omega}{Dt} = (\omega \cdot \nabla)\,\mathbf{u} + \nu\nabla^2\omega \tag{33}$$

Two effects which will be at play in three dimensions are not apparent in our two dimensional approximation. The first term on the right hand side of equation 33 represents vortex stretching. Assuming an axisymmetric ring, the z component of this term is $\omega_z \frac{\partial u_z}{\partial z}$ for the planar slice we have simulated. The relative magnitude of this term should vary inversely with vortex size and be roughly proportional to vortex strength. The second term, $\nu\nabla^2\omega$, is the diffusion of vorticity. In a vortex ring, local bubble induced distortion could diffuse (and extend itself) in the third (ring) direction, potentially creating more complex disturbances than those predicted by the present simulation.

Ferrante & Elghobashi[4] offer some interesting commentary in their study of micro-bubbles in Taylor-Green vortex flow. The authors neglected the influence of gravity, and simulated the microbubbles using a two fluid model. However, because there is no influence of gravity, and their bubble concentration is much higher than this study, the observed effects differ somewhat. They showed that the fluid divergence, $\nabla \cdot \mathbf{u}$, caused by the presence of the bubbly phase, was the primary cause for an observed decrease in vorticity at the center of

the vortex. We notice a similar decrease in vorticity decay when the bubbles settle very close to the center (figures 16(b) and 17(b)). However, this decrease is always accompanied by a band with at least a slight increase of vorticity. As the effects of buoyancy pull larger bubbles away from the center, this effect is amplified. If gravity is neglected in the present work, bubbles would cluster at the vortex center and the results may resemble Ferrante and Elghobashi's.

V. A CORRELATION FOR DECAY OF ANGULAR MOMENTUM, E.

The results in table VII show that some combinations of bubble size and vortex strength result in significantly more vortex distortion than others, dependent on the measurement criteria. Increasing bubble size, thus decreasing the fluid volume fraction, seems to have an effect, as does changing the vortex strength. However there appears to be no straightforward way to explain variations in the relative decay rate, E, based on the handful of available variables. In this section, we develop an analysis to understand how this increase in the vortex decay rate scales with the magnitude of the highly local, bubble-fluid interactions.

We start by calculating the net reaction force acting on the fluid due to the presence of the bubbles with volumetric coupling. A similar analysis was conducted by S&K as well as Druzhinin & Elghobashi[8]. We will derive an expression here applicable to the current Eulerian-Lagrangian framework, and use it to calculate the net reaction from the entrained bubbles at their settling location in a Gaussian vortex. We can write the single phase, undisturbed momentum equation as:

$$\underbrace{\frac{\partial\left(\rho_\ell \mathbf{u}\right)}{\partial t}+\nabla\cdot\left(\rho_\ell \mathbf{u}\mathbf{u}\right)}_{\mathbf{C}}=\underbrace{-\nabla P}_{\mathbf{P}}+\underbrace{\nabla\cdot\left(\mu_f(\nabla\mathbf{u}+\nabla\mathbf{u}^T)\right)}_{\mathbf{V}}\underbrace{-\rho_\ell \mathbf{g}}_{\mathbf{B}},$$
$$\mathbf{C}=\mathbf{P}+\mathbf{V}+\mathbf{B}, \tag{34}$$

where $\mathbf{C}$ denotes the total acceleration term, $\mathbf{P}$ denotes the pressure term, $\mathbf{V}$ the viscous term, and $\mathbf{B}$ the gravitational body force term. Similarly for multiphase flow, the volume averaged momentum equation can be expressed as

$$\underbrace{\frac{\partial}{\partial t}\left(\rho_\ell \Theta_\ell \mathbf{u}_\ell\right)+\nabla\cdot\left(\rho_\ell \Theta_\ell \mathbf{u}_\ell \mathbf{u}_\ell\right)}_{\hat{\mathbf{C}}}=\underbrace{-\nabla P}_{\hat{\mathbf{P}}}+\underbrace{\nabla\cdot\left(\Theta_\ell \mu_\ell \mathbf{D}\right)}_{\hat{\mathbf{V}}}\underbrace{-\Theta_\ell \rho_\ell \mathbf{g}}_{\hat{\mathbf{B}}}+\mathbf{f}_{b\to\ell} \tag{35}$$
$$\hat{\mathbf{C}}=\hat{\mathbf{P}}+\hat{\mathbf{V}}+\hat{\mathbf{B}}+\mathbf{f}_{b\to\ell}$$

Here, $\hat{\mathbf{C}}$, $\hat{\mathbf{P}}$, $\hat{\mathbf{V}}$, and $\hat{\mathbf{B}}$ are the same contributions to the fluid momentum, but are representative of the disturbed flow field containing the eight finite size bubbles. Recall that $\mathbf{f}_{b\to\ell}$ is the interphase momentum exchange term which is not present in the single phase equations. If all terms are moved to the right hand side, and the single phase terms are subtracted from the disturbed flow terms, we can write an expression for the reaction force per unit volume ($\widehat{\Delta\mathbf{R}}$) imposed on the fluid by the presence of the bubbles:

$$\widehat{\Delta\mathbf{R}} = \left(\mathbf{C} - \hat{\mathbf{C}}\right) + \left(\hat{\mathbf{P}} - \mathbf{P}\right) + \left(\hat{\mathbf{V}} - \mathbf{V}\right) + \left(\hat{\mathbf{B}} - \mathbf{B}\right) + \mathbf{f}_{b\to\ell}. \tag{36}$$

In order to simplify this and arrive at an expression applicable to the present case, we make the following assumptions. First, the undisturbed flow is steady over the timescale of bubble to fluid momentum transfer. Second, the bubbles are not accelerating. Once they reach their settling location, they translate rectilinearly with the vortex core (see figure 13(b)). This also implies that the lift, drag, added mass, pressure, and gravity forces are in balance. Finally, we assume the vortex core is well represented by the axisymmetric, Gaussian profile. This was shown to be a good approximation for the present cases in figure 12. The advantage to this assumption is that we now have good estimates for velocity, vorticity, and dynamic pressure gradient at all positions in the vortex core. The individual terms in equation 36 can then be simplified as follows:

$$\begin{aligned}
&\mathbf{C} - \hat{\mathbf{C}} = \rho_\ell \frac{D\mathbf{u}}{Dt} - \frac{D\left(\Theta_\ell \rho_\ell \mathbf{u}\right)}{Dt} \approx \rho_\ell \frac{u_\theta^2}{r} - \rho_\ell \frac{\Theta_\ell u_\theta^2}{r} \approx \rho_\ell \Theta_b \frac{u_\theta^2}{r} \\
&\hat{\mathbf{P}} - \mathbf{P} = \nabla P - \nabla P = 0 \qquad (37) \\
&\hat{\mathbf{V}} - \mathbf{V} \approx \mu \nabla\left(\Theta_\ell \nabla \mathbf{u}\right) - \mu \nabla^2 \mathbf{u} \approx \text{assumed negligible if } \mu << 1 \\
&\hat{\mathbf{B}} - \mathbf{B} = -\Theta_\ell \rho_\ell \mathbf{g} + \rho_\ell \mathbf{g} = +\Theta_b \rho_\ell \mathbf{g} \qquad (38)
\end{aligned}$$

Also, since the bubbles reach a settling location that is steady with respect to the vortex core, the net forces on the bubble are in balance,

$$\begin{aligned}
\mathbf{F}_{\ell\to b} &= \left(\mathbf{F}_D + \mathbf{F}_L + \mathbf{F}_{AM} + \mathbf{F}_P\right) = -\mathbf{F}_G; \\
\mathbf{f}_{b\to\ell} &= -\sum_{b=1}^{N_b} \mathcal{G}_\Delta(\mathbf{F}_{\ell\to b}) = -\Theta_b \rho_b \mathbf{g}.
\end{aligned} \tag{39}$$

The change in fluid body force can be combined with the interphase reaction term, $\mathbf{f}_{b\to\ell}$, to form a net buoyancy force experienced by the fluid. Note that the interphase reaction term will be small when the bubbles are not accelerating, explaining why the point-particle,

two-way coupling approach causes almost no vortex distortion. The only other significant term which arises in this simplification is due to changes to the dynamic pressure gradient ($\rho_\ell u_\theta^2/r$). If all terms are combined, and we multiply through by the fluid volume, then the total reaction force ($\Delta\mathbf{R} = V_{cv}\widehat{\Delta\mathbf{R}}$) to the fluid because of N_b bubbles having volume V_b becomes:

$$\Delta\mathbf{R} = N_b V_b \left(\frac{\rho_\ell u_\theta^2}{r_s} + \mathbf{g}(\rho_\ell - \rho_b) \right) \tag{40}$$

This is in agreement with the general expression obtained by Druzhinin & Elghobashi for their two-fluid model, and used by S&K in their discussion of bubble induced vortex distortion. In order to find the magnitude of the total reaction to the fluid, we decompose the reaction into components. In a counter-clockwise cylindrical coordinate system (ccw rotation is positive, radially outward is positive) located at the vortex center we have,

$$R_r = N_b V_b \left[\mathbf{g}\left(\rho_\ell - \rho_b\right) \sin(\theta_s) - \frac{\rho_\ell u_\theta^2}{r_s} \right] \tag{41}$$

$$R_\theta = N_b V_b \mathbf{g}\left(\rho_\ell - \rho_b\right) \cos(\theta_s). \tag{42}$$

In the present clockwise vortices, the magnitude of this reaction will be directed up and to the left from the settling location in first quadrant. The magnitude and direction of the net reaction measured from the horizontal ($\theta = 0$) will be

$$R_{net} = \sqrt{R_r^2 + R_\theta^2} \tag{43}$$

$$\theta_R = \theta_s + \frac{\pi}{2} + \arctan\left(\frac{R_r}{R_\theta}\right) \tag{44}$$

We now seek a quantity which can make sense of the changes in vortex structure and decay rate for certain combinations of bubble size and initial vortex strength. The net reaction, R_{net}, represents a local input to the fluid. Intuitively, the local force which drives the rotation of the vortex should also dictate the magnitude of the effects. We therefore choose to normalize, R_{net}, by the local vortex force, F_{vx}^{local}. The idea of the vortex force was originally developed by Prandtl and is frequently used when studying vortex dynamics[41]. It can be thought of as the force required to maintain steady rotation of a vortex. It is defined for a closed region as

$$\mathbf{F}_{vx} = \int \mathbf{u} \times \omega \, dV \tag{45}$$

If we insert the expressions for the Gaussian vortex velocity and vorticity fields, we can obtain an expression for the total vortex force required to drive the Gaussian vortex having

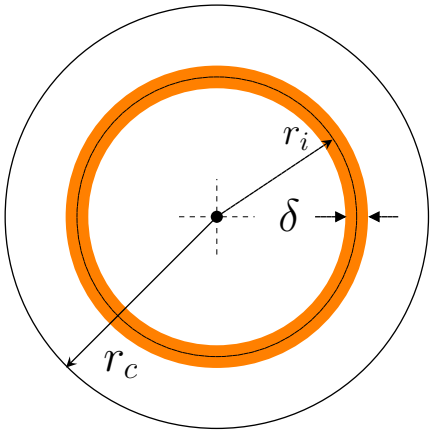

FIG. 19. Schematic of differential band used to integrate the local vortex force.

initial strength Γ_0 and core radius, r_c.

$$F_{vx} = \frac{\Delta z \Gamma_0^2 \eta_1}{2\pi r_c^2} \int_0^{r_c} \left[e^{-\eta_1 (r/r_c)^2} - e^{-2\eta_1 (r/r_c)^2} \right] dr \tag{46}$$

Here, the cross product in the integral has been simplified because the velocity (u_θ) is orthogonal to the vorticity (ω_z) at all points in the undisturbed, 2D vortex core. The integration variable has been changed from the vortex volume to the vortex radius. Using this expression, a more helpful quantity is the vortex force required to maintain rotation of a small band centered at the bubble settling radius, illustrated schematically in figure 19. By changing the integration limits in equation 46 to represent a band of width δ, centered at the bubble settling radius, r_s, we obtain

$$F_{vx}^{local} = \frac{\Delta z \sqrt{2\eta_1} \Gamma_0^2}{8\sqrt{\pi} r_c} \left[\sqrt{2}\, \mathrm{erf}\left(\sqrt{\eta_1} \frac{r}{r_c} \right) - \mathrm{erfc}\left(\sqrt{2\eta_1} \frac{r}{r_c} \right) \right]_{r_s - \frac{\delta}{2}}^{r_s + \frac{\delta}{2}} \cdot \frac{r_c}{\delta} \tag{47}$$

Note, that the integration has been post-multiplied by the scaling quantity r_c/δ. This is to account for the effect that choice of bandwidth has on the magnitude of the integral. By rescaling in this way, the values of vortex force become independent of the choice of δ so long as $\delta << r_c$.

Figure 20 shows how the magnitude of the local vortex force changes with radius in the core of the Gaussian vortex for the three different initial strengths considered. From equation 47, we see that the force scales quadratically with the vortex strength. The local vortex force is minimized by decreasing strength or increasing radius. Using the bubble settling coordinates, the net reaction, R_{net} and local vortex force, F_{vx}^{local}, are calculated

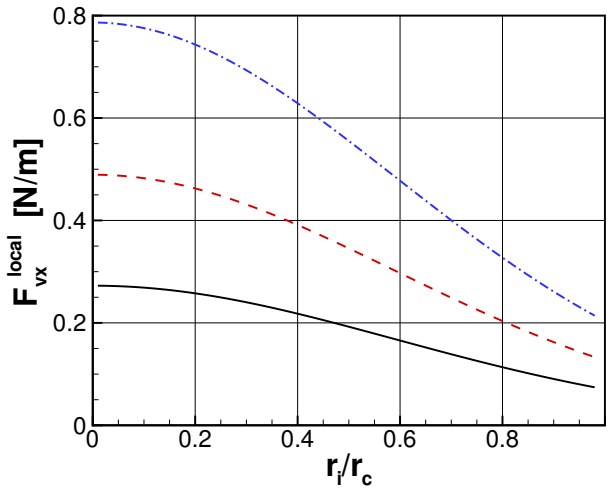

FIG. 20. Local vortex force calculated by equation 47 for a band of width and thickness δ as illustrated in figure 19. (—)$\Gamma_0 = 0.0159\ m^2/s$, (- - -)$\Gamma_0 = 0.0206\ m^2/s$, (-·-)$\Gamma_0 = 0.0254\ m^2/s$

for each of the 12 cases with volumetric coupling. The net reaction is then normalized by the local vortex force to compute a relative reaction force, $R_{rel} = R_{net}/F_{vx}^{local}$. This relative reaction force can be thought of as a potential for vortex distortion, or momentum redistribution. The relative decrease in vortex decay rate, E, is plotted against R_{rel} in figure 21. The figure shows that the relative reaction force is capable of both collapsing the values of E and also producing a highly linear trend across the data points. There are two important implications of this result. First, we see that the local vortex force is a valuable scaling parameter for normalizing the interphase reaction force. Determining a local measure of the vortex force in this case was straightforward because of the good match with the Gaussian flow field. For an arbitrary flow field such as homogeneous turbulence, a more general approach is needed. Second, we have obtained a correlation between a large scale vortex property, E, and a property associated with the local bubble-scale interactions, R_{rel}. This could be coupled with a model for the settling coordinates such as the one developed in section III A, to arrive at a lower order model for bubble induced vortex attenuation based solely on the parameters Γ_0, r_c, and d_b.

VI. CONCLUSIONS

The entrainment of small bubbles into both stationary and traveling, two dimensional vortex tubes has been investigated using a Discrete Element Model. In this Eulerian-Lagrangian

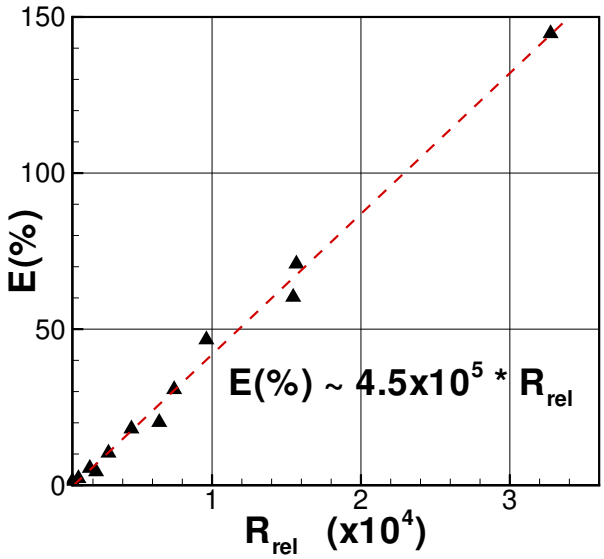

FIG. 21. Linear relationship between E and R_{rel} for each of the 12 cases simulated with volumetric coupling.

approach, solution to the carrier phase is obtained using direct numerical simulation whereas motion of subgrid bubbles is modeled using Lagrangian tracking. Three bubble-fluid coupling approaches were investigated to study bubble-vortex interactions: (i) passive one-way coupling wherein the bubble motion is affected by the fluid but the bubbles do not affect the flow, (ii) point-particle two-way coupling wherein the bubbles affect the fluid flow through a reaction force in the momentum equation, and (iii) finite-size volumetric coupling wherein the *volumetric displacement* of the fluid by the finite size of the bubbles is modeled along with interphase momentum-exchange for a realistic coupling of the bubbles to the carrier phase. The accuracy of the numerical implementation was first verified by simulating bubble motions in a stationary Gaussian vortex for passive one-way coupling. Results were compared with analytic expressions for the bubble settling locations derived using an extension of the force balance method of Van Nierop et al.[3]. The accuracy of the reaction force coupling as well as volumetric displacement effects were investigated by simulating bubble entrainment in a Rankine vortex. Grid and time-step refinement studies were conducted to show second order accuracy.

The validated numerical approach was then applied to investigate bubble-vortex interactions in a traveling vortex at very low overall volume loading. Due to the low overall volume fraction and strength of the vortex considered, the two-way coupling model results

in almost no effect on the fluid phase. In this case, the volumetric coupling model is critical for both predicting the correct bubble settling location, and capturing the bubble induced vortex distortion. The strong lift coefficient suggested by Sridhar & Katz results in excellent experimenal agreement in settling location when combined with the volumetric coupling model. This suggests that the experimentally measured lift coefficient is strongly dependent on local changes to the flowfield induced by bubble motion through volumetric coupling. These changes (vortex distortion) were assessed using measurements of relative asymmetry and core fragmentation, peak vorticity, and angular momentum decay rate. To better understand why the magnitude of these changes varried case to case, a method for determining a relative reaction force, or distortion potential was developed using the idea of a local vortex force. This potential can be thought of as the relative ability of the bubbles to cause change to the vortex flow structure. For the Gausian type vortices studied in this work, it is based entirely on the bubble size, vortex size, the vortex strength. The results show a linear correlation between this distortion potential and the observed relative increase in the vortex decay rate. This important relationship shows how local bubble scale interactions can be related to vortex scale strength attenuations. This study may have important consequences in understanding bubble interactions with coherent vortical structures in turbulent flows.

ACKNOWLEDGMENTS

This work was supported in part by the Office of Naval Research (ONR grant number N000140610697) and in part by Department of Energy's National Energy Technology Laboratory (Contract number 41817M4077). Authors thank Dr. Ki-Han Kim of ONR for support from ONR. JF and SVA also thank DoE and Dr. Cathy Summers (NETL, Albany) for partial support. All simulations were performed on the high performance computing cluster at Oregon State University.

Appendix: Numerical Methods

The fluid flow solver is based on a co-located grid finite volume scheme for arbitrary shaped unstrcutured grids[34,42]. The details of the numerical implementation are given in[35]. Here we summarize the basic steps for completeness.

1. Variable Storage

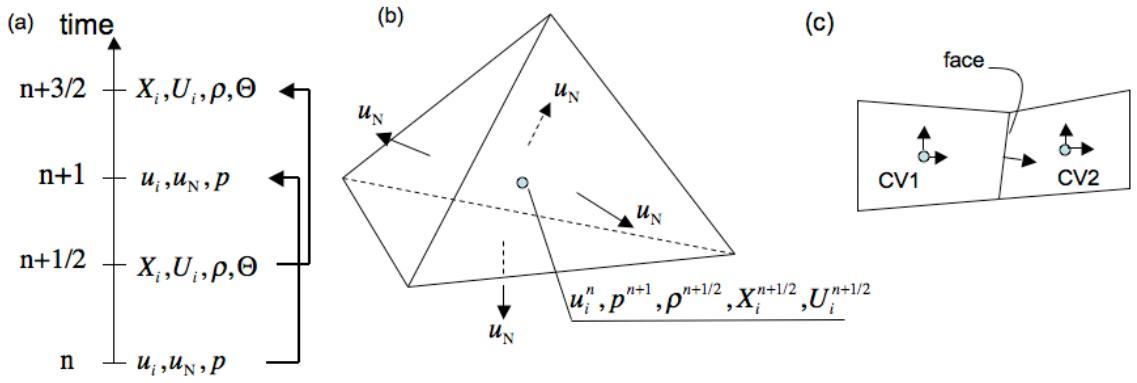

FIG. 22. Schematic of the grid stencil: (a) time staggering of variables, (b) velocity (u_i) and pressure fields (p) are colocated at the control volume center, u_N is the face-normal velocity, (c) control volume and face connectivity.

Figure 22 shows the schematic of variable storage in time and space. The dispersed phase positions, density, pressure and volume fractions are staggered in time with respect to the fluid and particle velocity fields, u_i and U_i, respectively. All variables are stored at the control volume (cv) center with the exception of the face-normal velocity u_N, located at the face centers. The face-normal velocity is used to enforce continuity equation. Capital letters are used to denote disperse phase. The time-staggering is done so that the variables are located most conveniently for the time-advancement scheme. We follow the collocated spatial arrangement for velocity and pressure field as has been used by [42–44]. The main reason to use this arrangement as opposed to spatial-staggering is its easy application to unstructured grids and/or adaptive mesh refinement. Accordingly, the dispersed phase positions (X_i), density (ρ), volume fraction (Θ), and viscosity (μ) are located at time level $t^{n+1/2}$ and $t^{n+3/2}$ whereas the fluid velocity (u_i, u_N) and the dispersed phase velocity (U_i), and the pressure (p) are located at time level t^n and t^{n+1}. This makes the discretization symmetric in time, a feature important to obtain good conservation properties of the numerical scheme as emphasized and used by Pierce and Moin[45] for low-Mach number, reactive flows.

2. Numerical Algorithm

The goal is to advance the flow solution from t^n to t^{n+1}, and the dispersed phase solution from $t^{n+1/2}$ to $t^{n+3/2}$. Given proper specification of initial conditions, the solution proceeds as follows:

- **Step 1:** Advance the bubble positions and velocities using the adaptive time-stepping algorithm described above. Compute the void fraction field at the new bubble locations using the Lagrangian-Eulerian interpolation kernel and set the density $\rho = \rho_\ell \Theta_\ell$.

- **Step 2:** Advance the fluid momentum equations using the fractional step algorithm, with the interphase force, f_i, treated explicitly (the subscript ℓ for fluid phase is dropped for simplicity).

$$\frac{\rho_{\rm cv}^{n+1} u_i^* - \rho_{\rm cv}^n u_i^n}{\Delta t} + \frac{1}{2V_{\rm cv}} \sum_{\text{faces of cv}} \left[\rho_{\rm face}^{n+1} u_{i,\rm face}^* + \rho_{\rm face}^n u_{i,\rm face}^n\right] u_{\rm N}^{n+1/2} A_{\rm face} =$$
$$-\frac{\delta p}{\delta x_i}^n + \frac{1}{2V_{\rm cv}} \sum_{\text{faces of cv}} \mu_{\rm face}^* \left(\frac{\partial u_{i,\rm face}^*}{\partial x_j} + \frac{\partial u_{j,\rm face}^n}{\partial x_i}\right) A_{\rm face} + f_i^{n+1/2}, \quad \text{(A.1)}$$

  where N is the face-normal component, and $A_{\rm face}$ is the face area. The density fields at faces are obtained using simple arithmetic averages of density at adjacent CVs. Here the fluid viscosity is given as $\mu_{\rm face}^* = \Theta_{\ell,\rm face} \mu_{\rm eff,face}$ where $\mu_{\rm eff}$ is the summation of the dynamic viscosity and eddy viscosity obtained from the dynamic Smagorinsky model. The pressure gradient at the CV centers in the above equation is at the old time-level and is obtained as described below. The reaction force $f_i^{n+1/2}$ is obtained through Lagrangian-Eulerian interpolation and consists of the pressure force on the disperse phase. In the above step, the viscous terms are treated implicitly, the three equations for the velocity components at the CV centers are solved using iterative scheme such as Gauss-Seidel.

- **Step 3:** Remove the old pressure gradient to obtain the velocity field, $\widehat{u}_i$:

$$\frac{\rho_{\rm cv}^{n+1} \widehat{u}_i - \rho_{\rm cv}^{n+1} u_i^*}{\Delta t} = +\frac{\delta p}{\delta x_i}^n \quad \text{(A.2)}$$

- **Step 4:** Interpolate the velocity fields to the faces of the control volumes and consider the corrector step:

$$\frac{\rho_{\rm face}^{n+1} u_{\rm N}^{n+1} - \rho_{\rm face}^{n+1} \widehat{u}_{\rm N}}{\Delta t} = -\frac{\delta p}{\delta x_{\rm N}}^{n+1}, \quad \text{(A.3)}$$

where $\widehat{u}_{\mathrm{N}} = \widehat{u}_{i,\mathrm{face}}\mathrm{N}_{i,\mathrm{face}}$ is the approximation for face-normal velocity and $\mathrm{N}_{i,\mathrm{face}}$ are the components of the face-normal. To compute the face-based pressure gradient, we make use of the face and its two adjacent CVs (CV1 and CV2) as shown in figure 22c. The face-normal pressure gradient is discretized as:

$$\frac{\delta p}{\delta x_{\mathrm{N}}}^{n+1} = \frac{p_{\mathrm{nbr}}^{n+1} - p_{\mathrm{cv}}^{n+1}}{|\mathbf{S}_{\mathrm{cv}\to\mathrm{nbr}}|}, \tag{A.4}$$

where the subscripts cv and nbr stand for the the control volume CV for which the velocity field is being solved and the neighboring CV sharing a common face, respectively and $|\mathbf{S}_{\mathrm{cv}\to\mathrm{nbr}}|$ represents the magnitude of the vector connecting the two control volumes.

- **Step 5:** The pressure field and the pressure gradients at t^{n+1} are unknown in the above step. A pressure Poisson equation is derived by taking a discrete divergence of the above equations and solving for the pressure field at each control volume:

$$\sum_{\text{face of cv}} \Delta t \frac{\delta p}{\delta x_N}^{n+1} = \sum_{\text{faces of cv}} \rho_{\mathrm{face}}^{n+1} \widehat{u}_{i,\mathrm{face}} A_{\mathrm{face}} + V_{\mathrm{cv}} \frac{\rho_{\mathrm{cv}}^{n+3/2} - \rho_{\mathrm{cv}}^{n+1/2}}{\Delta t}. \tag{A.5}$$

- **Step 6:** Reconstruct the pressure gradient at the CV centers. The face-normal pressure gradient $\frac{\delta p}{\delta x_N}$ and the gradient in pressure at the CV-centroids are related by the area-weighted least-squares interpolation[42,44]:

$$\epsilon_{cv} = \sum_{\text{faces of cv}} \left(P'_{i,\mathrm{cv}}\mathrm{N}_{i,\mathrm{face}} - P'_{\mathrm{face}}\right)^2 A_{\mathrm{face}}, \tag{A.6}$$

where $P'_{i,\mathrm{cv}} = \frac{\delta p}{\delta x_i}$ and $P'_{\mathrm{face}} = \frac{\delta p}{\delta x_{\mathrm{N}}}$.

- **Step 7:** Compute new face-based velocities, and update the CV-velocities:

$$u_{\mathrm{N}}^{n+1} = \widehat{u}_{\mathrm{N}} - \frac{\Delta t}{\rho_{\mathrm{face}}^{n+1}} \frac{\delta p}{\delta x_{\mathrm{N}}}^{n+1} \tag{A.7}$$

$$u_{i,\mathrm{cv}}^{n+1} = \widehat{u}_{i,\mathrm{cv}} - \frac{\Delta t}{\rho_{\mathrm{cv}}^{n+1}} \frac{\delta p}{\delta x_{i,\mathrm{cv}}}^{n+1} \tag{A.8}$$

3. Interpolation Operator for Lagrangian-Eulerian Mapping

In the simulation of a coupled liquid and bubble system, mapping data from Eulerian framework (liquid phase) to Lagrangian framework (bubble/particle phase) is necessary. In

the Lagrangian calculation, data sets such as flow velocity, pressure, acceleration, etc., are needed for the bubble/particle motion. On the other hand, reaction forces acting on liquid phase and bubble volume fraction are needed to be mapped into Eulerian framework.

The interpolation function should be smooth and conserve the transferred variable[46]. In an orthogonal structured computational grid, linear or bilinear interpolation technique can be applied, depending on the level of accuracy needed. Snider *et al.*[47] used a trilinear interpolation technique in a staggered grid computation. McDermott and Pope[48] have recently proposed the Parabolic Edge Reconstruction Method (PERM) for continuous velocity field reconstruction in the subgrid level. Kernel-based interpolation techniques, typical of particle methods, can be easily applied to complex and unstructured grids. Different interpolation kernels using polynomial[32,49] or exponential[50,51] function formulation have been used. Gaussian kernel provides quadrature spectral accuracy, provided that the interpolation is being performed over a region much larger than the kernel width[50], otherwise the accuracy reduces to second order. They do not have a compact support, but are smooth, accurate and easy for use on unstructured grids.

The Gaussian interpolation function is given by

$$\mathcal{G}_\Delta(\mathbf{x}, \mathbf{x}_b) = \frac{1}{\left(\sigma\sqrt{(2\pi)}\right)^3} \exp\left[-\frac{\sum_{k=1}^{3}(x_k - x_{b,k})^2}{2\sigma^2}\right], \tag{A.9}$$

where σ is the kernel width, x_k and $x_{b,k}$ denote the available data point on the grid and the bubble location, respectively. In order to enforce mass conservation, the kernel function is normalized over the volume of integration by

$$\int_{V_{cv}} \mathcal{G}_\Delta(\mathbf{x}_{cv}, \mathbf{x}_b) dV = 1. \tag{A.10}$$

Using the above kernel, volume fraction of the liquid can be calculated as

$$\Theta_\ell = 1 - \sum_{i=1}^{n_b} V_b \mathcal{G}_\Delta. \tag{A.11}$$

REFERENCES

[1]G. Sridhar and J. Katz, "Effect of entrained bubbles on the structure of vortex rings," Journal of Fluid Mechanics, **397**, 171–202 (1999)

[2]G. Oweis, I. van der Hout, C. Iyer, G. Tryggvason, and S. Ceccio, "Capture and inception of bubbles near line vortices," Physics of Fluids, **17**, 022105 (2005)

[3]E. Van Nierop, S. Luther, J. Bluemink, J. Magnaudet, A. Prosperetti, and D. Lohse, "Drag and lift forces on bubbles in a rotating flow," Journal of Fluid Mechanics, **571**, 439–454 (2007)

[4]A. Ferrante and S. Elghobashi, "On the effects of microbubbles on taylor–green vortex flow," J. Fluid Mech., **572**, 145–177 (2007)

[5]G. Sridhar and J. Katz, "Drag and lift forces on microscopic bubbles entrained by a vortex," Physics of Fluids, **7**, 389 (1995)

[6]M. Maxey and J. Riley, "Equation of motion for a small rigid sphere in a nonuniform flow," Physics of Fluids, **26**, 883 (1983)

[7]G. Tryggvason, B. Bunner, A. Esmaeeli, D. Juric, N. Al-Rawahi, W. Tauber, J. Han, S. Nas, and Y. Jan, "A front-tracking method for the computations of multiphase flow," Journal of Computational Physics, **169**, 708–759 (2001)

[8]O. Druzhinin and S. Elghobashi, "Direct numerical simulations of bubble-laden turbulent flows using the two-fluid formulation," Physics of Fluids, **10**, 685 (1998)

[9]A. Prosperetti and D. Zhang, "Finite-particle-size effects in disperse two-phase flows," Theoretical and Computational Fluid Dynamics, **7**, 429–440 (1995)

[10]D. Joseph, T. Lundgren, R. Jackson, and D. Saville, "Ensemble averaged and mixture theory equations for incompressible fluid-particle suspensions," Int. J. Multiphase Flow, **16**, 35–42 (1990)

[11]M. van der Hoef, M. van Sint Annaland, N. Deen, and J. Kuipers, "Numerical Simulation of Dense Gas-Solid Fluidized Beds: A Multiscale Modeling Strategy," Annual Review of Fluid Mechanics, **40**, 47 (2008)

[12]D. Snider, "An incompressible three-dimensional multiphase particle-in-cell model for dense particle flows," Journal of Computational Physics, **170**, 523–549 (2001)

[13]N. Patankar and D. Joseph, "Modeling and numerical simulation of particulate flows by the Eulerian-Lagrangian approach," International Journal of Multiphase Flow, **27**, 1659–1684 (2001)

[14]N. Patankar and D. Joseph, "Lagrangian numerical simulation of particulate flows," International Journal of Multiphase Flow, **27**, 1685–1706 (2001)

[15]S. Apte, K. Mahesh, and T. Lundgren, "Accounting for finite-size effects in simulations

of disperse particle-laden flows," International Journal of Multiphase Flow (2007)

[16]A. Vreman, B. Geurts, N. Deen, and J. Kuipers, "Large-Eddy simulation of a particle-laden turbulent channel flow," in *Direct and large-eddy simulation V: proceedings of the fifth international ERCOFTAC Workshop on Direct and Large-eddy simulation, held at the Munich University of Technology, August 27-29, 2003* (Springer Netherlands, 2004) p. 271

[17]H. Jakobsen, B. Sann, S. Grevskott, and H. Svendsen, "Modeling of vertical bubble-driven flows," Ind. Eng. Chem. Res, **36**, 4052–4074 (1997)

[18]A. Ferrante and S. Elghobashi, "On the accuracy of the two-fluid formulation in direct numerical simulation of bubble-laden turbulent boundary layers," Physics of Fluids, **19**, 045105 (2007)

[19]I. Mazzitelli, D. Lohse, and F. Toschi, "The effect of microbubbles on developed turbulence," Physics of Fluids, **15**, L5 (2002)

[20]A. Ferrante and S. Elghobashi, "On the physical mechanisms of two-way coupling in particle-laden isotropic turbulence," Physics of Fluids, **15**, 315 (2003)

[21]E. Climent, M. Simonnet, and J. Magnaudet, "Preferential accumulation of bubbles in Couette-Taylor flow patterns," Physics of Fluids, **19**, 083301 (2007)

[22]L. Schiller and A. Naumann, "A drag coefficient correlation," Vdi Zeitung, **77**, 318–320 (1935)

[23]T. Auton, "The lift force on a spherical body in a rotational flow," Journal of Fluid Mechanics Digital Archive, **183**, 199–218 (2006)

[24]D. Dandy and H. Dwyer, "A sphere in shear flow at finite Reynolds number: effect of shear on particle lift, drag, and heat transfer," Journal of Fluid Mechanics, **216**, 381–410 (2006)

[25]Note the expression for C_L here has been algebraically manipulated from the one originally published by S&K[5] in order to be consistent with the definition of lift force used here and by Van Nierop et al.[3]

[26]C. Crowe, M. Sommerfeld, and Y. Tsuji, *Multiphase Flows with Droplets and Particles* (CRC Press, 1998)

[27]D. Darmana, N. Deen, and J. Kuipers, "Parallelization of an Euler–Lagrange model using mixed domain decomposition and a mirror domain technique: Application to dispersed gas–liquid two-phase flow," Journal of Computational Physics, **220**, 216–248 (2006)

[28]R. Jackson, "Locally averaged equations of motion for a mixture of identical spherical particles and a Newtonian fluid," Chemical Engineering Science, **52**, 2457–2469 (1997)

[29]D. Zhang and A. Prosperetti, "Momentum and energy equations for disperse two-phase flows and their closure for dilute suspensions," International Journal of Multiphase Flow, **23**, 425–453 (1997)

[30]D. Gidaspow, *Multiphase Flow and Fluidization: Continuum and Kinetic Theory Descriptions* (Academic Press, 1994)

[31]J. A. M. Kuipers, K. J. van Duin, F. P. H. van Beckum, and W. P. M. van Swaaij, "Computer simulation of the hydrodynamics of a two-dimensional gas-fluidized bed," *An International Journal of Computer Applications in Chemical Engineering*, Computers & Chemical Engineering, **17**, 839–858 (1993)

[32]D. Darmana, N. G. Deen, and J. A. M. Kuipers, "Parallelization of an euler-lagrange model using mixed domain decomposition and a mirror domain technique: Application to dispersed gas-liquid two-phase flow," J. Comput. Phys., **220**, 216–248 (2006)

[33]K. Hutter and K. Jöhnk, *Continuum methods of physical modeling* (Springer, 2004)

[34]P. Moin and S. Apte, "Large-Eddy Simulation of Realistic Gas Turbine-Combustors," AIAA Journal, **44**, 698–708 (2006)

[35]E. Shams Sobhani, *Numerical simulation of cavitating bubble-laden turbulent flows*, Ph.D. thesis, Oregon State University (2010)

[36]E. Shams, J. Finn, and S. Apte, "A Numerical Scheme for Euler-Lagrange Simulation of Bubbly Flows in Complex Systems," International Journal of Numerical Methods in Fluids, **Accepted for Publication** (2010)

[37]C.-T. Hsiao, G. L. Chahine, and H.-L. Liu, "Scaling effect on prediction of cavitation inception in a line vortex flow," J. Fluids Eng., **125**, 53–60 (2003)

[38]S. James and C. Madnia, "Direct numerical simulation of a laminar vortex ring," Physics of Fluids, **8**, 2400 (1996)

[39]A. Glezer, "The formation of vortex rings," Physics of Fluids, **31**, 3532 (1988)

[40]J. Finn, "A multiscale modeling approach for bubble-vortex interactions in hydropropulsion systems," Ph.D. Thesis, Oregon State University (2009)

[41]P. Saffman, *Vortex dynamics* (Cambridge University Press, 1995)

[42]K. Mahesh, G. Constantinescu, S. Apte, G. Iaccarino, F. Ham, and P. Moin, "Large-eddy simulation of reacting turbulent flows in complex geometries," J. Appl. Mech, **73**, 374

(2006)

[43]D. Kim and H. Choi, "A second-order time-accurate finite volume method for unsteady incompressible flow on hybrid unstructured grids," J. Comput. Phys., **162**, 411–428 (2000)

[44]K. Mahesh, G. Constantinescu, and P. Moin, "A numerical method for large-eddy simulation in complex geometries," J. Comput. Phys., **197**, 215–240 (2004)

[45]C. D. Pierce and P. Moin, "Progress-variable approach for large-eddy simulation of non-premixed turbulent combustion," J. Fluid Mech., **504**, 73–97 (2004)

[46]A. Kitagawa, Y. Murai, and F. Yamamoto, "Two-way coupling of eulerian-lagrangian model for dispersed multiphase flows using filtering functions," Int. J. Multiphase Flow, **27**, 2129–2153 (2001)

[47]D. M. Snider, "An incompressible three-dimensional multiphase particle-in-cell model for dense particle flows," J. Comput. Phys., **170**, 523–549 (2001)

[48]R. McDermott and S. B. Pope, "The parabolic edge reconstruction method (perm) for lagrangian particle advection," J. Comput. Phys., **227**, 5447–5491 (2008)

[49]N. G. Deen, M. van Sint Annaland, and J. A. M. Kuipers, "Multi-scale modeling of dispersed gas-liquid two-phase flow," Chem. Engng. Sci., **59**, 1853 – 1861 (2004), ISSN 0009-2509, complex Systems and Multi-scale Methodology

[50]J. Eldredge, A. Leonard, and T. Colonius, "A general deterministic treatment of derivatives in particle methods," J. Comput. Phys., **180**, 686–709 (2002)

[51]S. V. Apte, M. Gorokhovski, and P. Moin, "Les of atomizing spray with stochastic modeling of secondary breakup," Int. J. Multiphase Flow, **29**, 1503–1522 (2003)